2
Phase Transitions in Two-Dimensional Colloidal Systems

H. H. von Grünberg, P. Keim, and Georg Maret

Abstract

This chapter is an introduction to phase transitions in two-dimensional (2D) systems. In contrast to three dimensions (3D), microscopic theories of melting exist in 2D. The most well known of them was developed more than 30 years ago by Kosterlitz, Thouless, Halperin, Nelson, and Young (KTHNY theory). This theory predicts the unbinding of topological defects to break the symmetry in two steps at two distinct temperatures. Dissociation of dislocation pairs first melts the crystal into a still orientationally ordered (hexatic) phase and, in the second step, dissociation of free dislocations causes the system to go over to an isotropic fluid. Colloidal systems are used to verify experimentally the predictions of KTHNY theory in detail as colloids provide the possibility to visualize the change in symmetry on an "atomic" level by simple video-microscopy. Elastic moduli like Young's modulus and Frank's constant are deduced from microscopic trajectories of colloids in order to quantify the softening of the 2D ensemble in the vicinity of the phase transitions.

2.1
Introduction

The macroscopic physical properties of matter depend on the interactions between atoms and/or molecules, on their spatial arrangement, and on temperature. A – sometimes subtle – balance between internal energy and entropy dictates the thermodynamic phase behavior of the bulk material. Depending on temperature, pressure or density, different phases may appear with completely different responses to external factors: response functions such as magnetic susceptibility, mechanical compressibility or shear modu-

Soft Matter, Vol. 3: Colloidal Order from Entropic and Surface Forces
Edited by G. Gompper and M. Schick

ISBN: 978-3-527-31370-9

lus may differ greatly in the high- and low-temperature phase. As a rule the high-temperature phase is always more symmetric than the low-temperature phase. In a fluid, for instance, the positions of the atoms are randomly distributed and no position is more likely than any other. At macroscopic scales the fluid therefore looks the same at every position, indicating continuous translational and orientational symmetry. By lowering the temperature T of the fluid, the translational degrees of freedom of individual particles become restricted. The system can lower its free energy $F = U - TS$ by introducing order. The corresponding loss of entropy S (that enters the free energy F with a negative sign, thereby leading to an increase of free energy) is overcompensated by the reduction of the internal energy U: potential energy wins against thermal energy. Another well-known example is the para- to ferromagnetic transition, where random, totally symmetric directions of the elementary atomic moments in the high-T phase spontaneously align in the magnetic low-T phase.

In both of our examples a symmetry is broken due to ordering: the magnetic moments start to orient parallel in magnetic systems so rotational invariance is broken, and atoms arrange in close-packed periodic structures where continuous translational and orientational symmetries are broken in favor of discrete ones. It is a general feature of phase transitions that high symmetry in the high-temperature phase is broken in one or several steps until a low-temperature phase with low symmetry occurs. Note, however, as an exception, that the common transition between a liquid and a gas which are both high-symmetry phases does not obey this principle, but above the critical point these two phases with the same symmetry are indistinguishable anyway, so we may consider both as a fluid.

The concept of macroscopic symmetry breaking does not tell us anything about how a particular system manages to do so on the atomic scale. In fact, the microscopic processes involved in both melting and freezing are still poorly understood in many systems, despite their importance in the fabrication and properties of most solid materials. As a general concept, during heating of the system, increasing amounts of defects in the ordered phase and dynamical (vibrational) modes provide the tools to restore symmetry. The dynamical modes depend strongly on the phase itself and are connected to the corresponding response functions, which are thus strongly dependent on temperature. In a liquid, for instance, sound wave propagation is not transverse but longitudinal since there is no shear modulus but there is a compression modulus.

In order to calculate the properties of matter from a microscopic point of view, one has to consider a huge amount of particles, typically of the order 10^{25} (e.g. in a liter of water). This, combined with the fact that one has to deal with singularities, for instance to describe a jump in the specific heat, makes

it impossible to solve the equations of state to describe phase transitions for any three-dimensional model represented in Nature. Thus, phenomenological theories have been developed, with the perhaps surprising outcome that in the vicinity of the phase transition the microscopic interaction is ancillary. This is because large fluctuations in the order parameter which describe the magnitude of the symmetry-related order play an important role. The latter leads to so-called universality classes of phase transitions, which are characterized by a universal behavior irrespective of the microscopics, but rather just depend on the degrees of freedom of the system and on the dimension of the order parameter. This topic, which is most relevant for three-dimensional systems, is far beyond the scope of this chapter.

In this chapter we rather focus on systems in two dimensions where the situation is quite different and in fact much better understood. In 2D, no true long-range order exists due to long-wavelength fluctuations. This can be seen most easily from an argument given by Peierls (1935) for the magnetic XY model. Let us assume that we have N moments per system size L in one direction. For small relative rotations of neighboring magnetic moments $\delta\varphi$ around equilibrium, the interaction can be approximated by a harmonic potential. If the magnetic moments interact only with a finite number of neighbors, then the energy density of the mode with the longest wavelength is $\propto (2\pi/N)^2$. Here the angle of rotation between nearest neighbors is $\delta\varphi = 2\pi/N$. Summation over all N magnetic moments, varying from 0 to 2π from one side of the sample to the other (see Fig. 2.1) leads to an energy proportional to $L(2\pi/L)^2$ in one dimension. It is $L^2(2\pi/L)^2$ in two dimensions and $L^3(2\pi/L)^2$ in three dimensions. So in 1D and 2D energy does not diverge with system size and the long-wavelength modes will be activated at finite temperature.

A generalization of this argument for non-harmonic interactions was given by Mermin and Wagner (1966) and for lattice theories by Mermin (1968). The displacement $\vec{u}(\vec{R})$ of a particle diverges with distance $\vec{R}$ as

$$\langle[\vec{u}(\vec{R}) - \vec{u}(\vec{R}')]^2\rangle \sim \ln|\vec{R} - \vec{R}'| \qquad \text{for} \qquad |\vec{R} - \vec{R}'| \to \infty \tag{2.1}$$

where $\vec{R} = n_1\vec{a}_1 + n_2\vec{a}_2$ ($n_i \in \mathbb{N}$ and $\vec{a}_i$ primitive translation vector) is an ideal lattice site. Due to the weak logarithmic divergence, one can still talk of a crystal. The discrete translational order is quasi-long-range whereas the

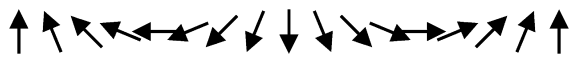

Fig. 2.1 One-dimensional wave of magnetic moments with lowest wavelength. The orientation angle of the moments varies in the range $[0, 2\pi]$ over the system size L.

discrete rotational symmetry is conserved. Therefore, unlike in 3D crystals, the structure factor

$$S(\vec{q}) = \frac{1}{N} \left\langle \sum_{\alpha,\alpha'} \mathrm{e}^{-\mathrm{i}\vec{q}(\vec{r}_\alpha - \vec{r}_{\alpha'})} \right\rangle \tag{2.2}$$

is not a set of delta peaks, but the peaks have a finite width and a particular q-dependent shape, which will be further discussed below.

In 2D systems a microscopic theory of melting was developed in the 1970s by Kosterlitz, Thouless, Halperin, Nelson, and Young (KTHNY theory). Melting is driven by the emergence – in the crystalline phase – of a class of topological defects, namely thermally activated dislocations pairs, which dissociate at the melting temperature T_m (Kosterlitz and Thouless 1973; Young 1979). This gives rise to a softening of the crystal's compressibility and shear elasticity, and the melting transition is a second-order transition. Nelson and Halperin predicted that the fluid phase above T_m still exhibits quasi-long-range orientational order with a sixfold symmetric director field (Halperin and Nelson 1978; Nelson and Halperin 1979). The orientational correlation function in this phase decays algebraically, which is associated with a non-vanishing elastic modulus of the orientational stiffness, called Frank's constant, K_A. Finally, at a temperature $T_\mathrm{i} > T_\mathrm{m}$ the orientational symmetry is broken upon the origination of a second class of topological defects: some of the dislocations dissociate into free disclinations, leading to another second-order transition and an exponential decay of the orientational correlation function above T_i. Now, the fluid shows ordinary short-range rotational and positional order as a characteristic of any isotropic liquid. The intermediate thermodynamic phase located between the isotropic liquid and the crystalline solid (which is unknown in 3D systems) is called hexatic. In order to visualize the different symmetries that we have just discussed, the structure factors of all three phases are shown in Fig. 2.2.

KTHNY is not the only melting scenario proposed so far for 2D systems. Alternative theoretical approaches such as grain-boundary-induced melting (Chui 1983; Kleinert 1983) or condensation of geometrical defects (Glaser and Clark 1993) suggest first-order transitions, and in Lansac et al. (2006) the effect of geometrical versus topological defects is discussed. Some numerical simulations indicate metastability of the hexatic phase (Chen et al. 1995; Somer et al. 1997) or a first-order melting transition (Jaster 1999). The latter is supposed to depend on finite-size effects (Mak 2006) in systems with hard-core interaction where fluctuations are believed to be very important. On the other hand, the effects of fluctuations seem less relevant in systems with a long-range pair potential. Indeed, recent simulations with dipole–dipole interactions clearly show second-order behavior (Lin et al. 2006).

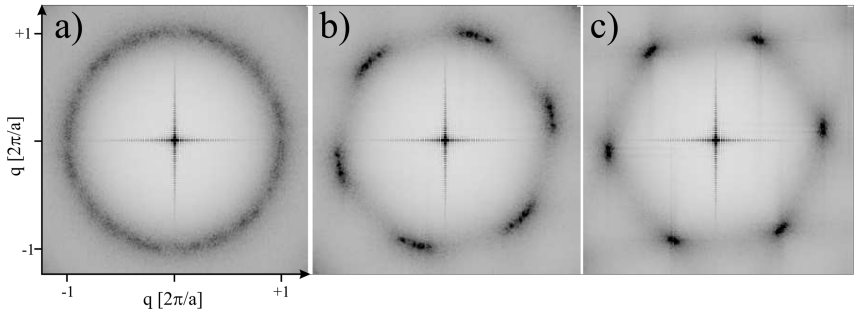

Fig. 2.2 Structure factor $S(q)$ of a colloidal system at various temperatures: (a) isotropic liquid, (b) hexatic phase, and (c) crystal (on the axes $a = 1/\sqrt{\rho}$ is the average interparticle distance, with ρ being the 2D density).

This chapter deals with phase transitions in two-dimensional systems. In Section 2.2 we outline the theory of dislocation-mediated melting. In Section 2.3 different experiments to verify the KTHNY theory are discussed and the unique advantages of colloidal 2D systems are highlighted. We focus on colloidal systems in Section 2.4 as they provide the possibility to visualize the ensemble at an "atomic" level. Trajectories of colloids can be recorded using video-microscopy and the change in symmetry at the phase transition can be observed directly. In particular, we emphasize experiments with colloids under magnetic dipole–dipole interactions confined at an absolutely smooth and flat surface because they provide the unique possibility to tune the system temperature in situ and to reach true thermodynamic equilibrium. This system turns out to be an ideal realization of a two-dimensional ensemble and the pair potential is known precisely. Due to these features these experiments have shown the most complete and quantitative evidence for KTHNY melting so far.

2.2
Theoretical Background

2.2.1
Dislocations and Disclinations in Two-Dimensional Crystals

A dislocation in a two-dimensional crystal is a defect that arises from the insertion of half lattice lines into the otherwise perfect lattice. Due to these lines a single dislocation cannot be made to disappear by any continuous transformation. This is why a dislocation is a topological defect. Figure 2.3 shows a dislocation in a square and in a triangular lattice, with the thick

dashed lines representing the inserted half lattice lines (two lines in the case of a hexagonal crystal due to symmetry, one line for a square one). From the sketch it is also evident how one can come back to the regular lattice: cutting the crystal along the hatched line, one has to relax the distorted lattice by shifting the whole lattice on one side of the cut by the vector $\vec{b}$ such that eventually the sites A and A′, B and B′, and C and C′ become connected again. This way of visualizing dislocations in solids is known as the Volterra construction, and the cut is termed the "Volterra cut" (Chaikin and Lubensky 1995).

The vector $\vec{b}$ is called the Burgers vector and is introduced to index the strength and orientation of a dislocation. A simple way to determine the Burgers vector of a dislocation is to draw a loop along a path that encloses the dislocation. This loop will contain an extra step corresponding to a direct lattice vector. This vector is the Burgers vector. In Fig. 2.3 such a Burgers circuit is completed following four steps along nearest-neighbor bonds in each of the lattice directions on a path around the dislocation. From this construction it is then clear that inserting two parallel half lines instead of one, one

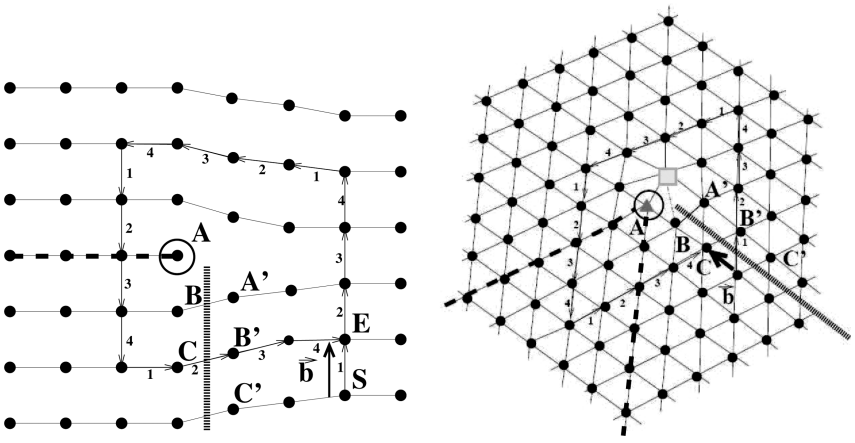

Fig. 2.3 Dislocations on square and triangular lattices arising from insertion of half lattice lines (thick dashed line with a circle indicating the tip of the inserted half line). The dislocation is characterized by a Burgers vector $\vec{b}$, which can be determined by considering a loop enclosing the dislocation. For the square lattice (left), starting from site S one follows the same number of steps along nearest-neighbor bonds that are made in each of the lattice directions in completing the circuit. The path ends at site E, which is not identical to S. Then $\vec{b}$ is the vector pointing from S to E. For the triangular lattice (right), $\vec{b}$ is obtained in the same way. Sixfold coordinated sites are plotted as filled circles, the sevenfold coordinated site as a square, and the fivefold coordinated site as a triangle. The regular lattice can be restored by cutting the crystal along the hatched bar putting A next to A′, B next to B′, and so forth.

would obtain a Burgers vector that is twice as long. In other words, a Burgers vector is a multiple of a direct lattice vector, with the multiplicity factor corresponding to the number of inserted parallel half lines. As Burgers vectors with multiplicity factors greater than one hardly ever occur in our systems, we will henceforth consider only dislocations with Burgers vectors of length a_0, where a_0 is the lattice constant. Then due to the symmetry of the lattice, there are only three Burgers vectors possible on a triangular lattice, and just two on a square lattice, one for each basic lattice vector. In the following we consider only the triangular lattice since it is the most densely packed one in 2D and favored by Nature.

The well-known Voronoi construction is used to determine the number of nearest neighbors of each site. This construction allows us to generate a mosaic from a given set of lattice sites. It assigns to each site a cell which is defined as the set of all points that are at least as close to this site as to any other site. Since the resulting Voronoi tessellation is an area-filling cellular structure, it allows us to introduce the notion of neighborhood, i.e. two sites are neighboring if their cells share at least one side. An example of such a Voronoi construction is given in Fig. 2.4b taken from Keim (2005). By means of such a Voronoi tessellation one can now determine the neighbor statistics for a triangular lattice hosting a dislocation. Figure 2.3 shows that the last site at the end of the inserted half line has only five rather than the usual six nearest neighbors. Next to this site, there is a sevenfold coordinated site. So, a dislocation can be viewed as a special kind of defect pair, a fivefold site being nearest neighbor to a sevenfold coordinated lattice site, where the vector $\vec{r}_{57}$ pointing along the bond connecting these two sites is almost perpendicular to the Burgers vector. A micrograph of a real two-dimensional crystal showing a dislocation is given in Fig. 2.4a.

Since the distortion of the lattice near a dislocation costs elastic energy, the probability of finding a dislocation in a crystal increases with temperature. This means that, even in crystals that are defect-free at zero temperature, dislocations have a chance of being formed at finite temperature. How is this sudden occurrence possible if the formation of a dislocation requires insertion of half a lattice line? The answer to this question is that single dislocations will never spontaneously form, but that dislocations will first appear in the form of dislocation pairs, which can then dissociate into single dislocations. And such pairs can evolve from local lattice displacements, as we now explain by means of Fig. 2.5.

Starting in Fig. 2.5 (left) from a perfect triangular lattice the sites A′ and B′ are displaced along a lattice line by a vector $\vec{d}$, while their nearest neighbors A and B on a line parallel to the first line are displaced by $-\vec{d}$. The distance $r_{\mathrm{BB}'}$ between B and B′ thus increases from a_0 to

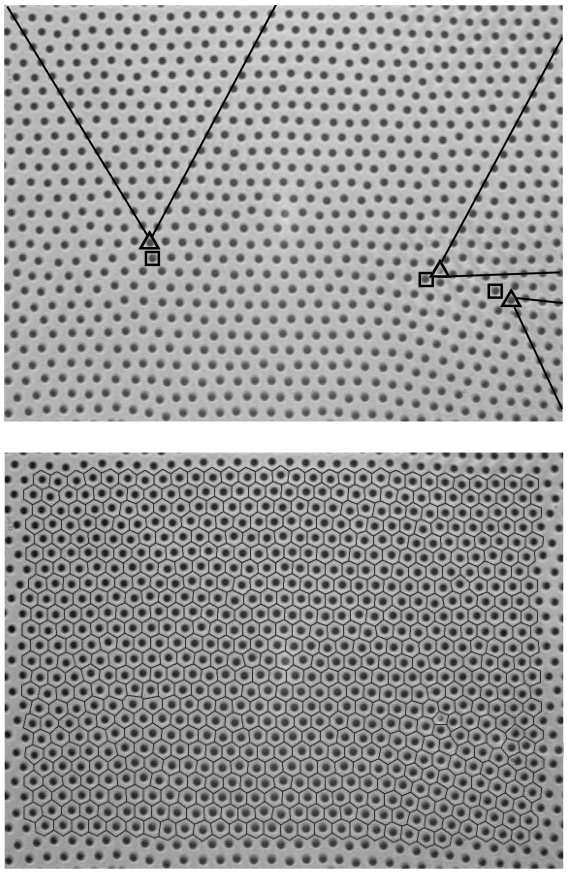

Fig. 2.4 (a) Micrograph ($420 \times 310\,\mu$m) of a colloidal crystal showing three isolated dislocations: the black squares mark the sevenfold coordinated colloids and the triangles mark the fivefold coordinated particles representing the end of the inserted half lattice lines (white solid lines). (b) By means of the Voronoi construction, the same area of the crystal is divided into cells, which allows us to determine the number of nearest neighbors of each particle.

$$r_{\mathrm{BB}'} = \sqrt{a_0^2 + (2d)^2 + 2da_0}$$

while the distance between A and A′ reduces from $\sqrt{3}\,a_0$ to

$$r_{\mathrm{AA}'} = \sqrt{3a_0^2 + (2d)^2 - 6da_0}$$

A Voronoi construction recognizes two sites as nearest neighbors if their distance is smaller than $\sqrt{7}\,a_0/2$. Once $d > a_0/4$ we find $r_{\mathrm{AA}'} < \sqrt{7}\,a_0/2$ and $r_{\mathrm{BB}'} > \sqrt{7}\,a_0/2$, meaning that the pair B and B′ then ceases to be nearest neighbors, while A and A′ are now allowed to become nearest neighbors. Hence, the effect of this coordinated shift through d is that B and B′ have lost

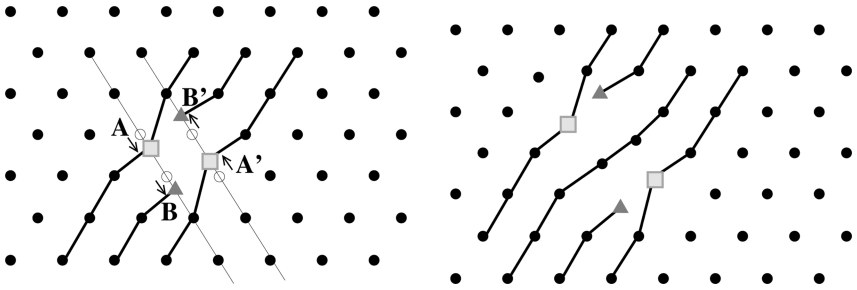

Fig. 2.5 Schematic drawing illustrating the formation and dissociation of dislocation pairs – see text. As in Fig. 2.3, sevenfold coordinated sites are plotted as squares, and fivefold coordinated sites as triangles.

a neighbor, and A and A′ have gained one, and that taken together two $(5,7)$ pairs have formed. This dislocation pair is bound at the smallest dislocation pair distance possible. If sufficient thermal energy is provided, the dislocation pair can be excited to a higher bound state in which the pair distance is larger, as depicted in Fig. 2.5 (right). Eventually this pair can completely dissociate into two dislocations. In this way two single dislocations are generated without there being the need to insert half lines. Note that the two dislocations in Fig. 2.5 have opposite Burgers vectors whose sum is zero. More generally we may conclude that a collection of dislocations whose sum of Burgers vectors vanishes can be obtained through a continuous transformation starting from a regular lattice.

With the decomposition of pairs into single dislocations, the decay of order is not yet completed: the next step that may occur if enough thermal energy is available is a dissociation of a single dislocation into an isolated fivefold coordinated site and another sevenfold coordinated site. These defects are disclinations. They form another class of topological defects in 2D solids. While for a dislocation the two sides of the Volterra cut have to be translated relative to each other, a disclination is obtained if the two sides are twisted relative to each other. For a triangular lattice there are just two angles through which the two sides can be rotated and still glued together, namely $+\pi/3$ and $-\pi/3$, resulting in the structures of Figs. 2.6 (a) and (c). Note that the positive disclination in (c) has a fivefold coordinated site at the core, while the negative disclination in (a) has a site that is sevenfold coordinated. Figure 2.6 (b), taken from Somer et al. (1997), shows a 2D system with four widely spaced disclinations, two positive ones in the upper left and lower right corners, and two negative ones in the upper right and lower left corners. It is evident that what has remained of the crystalline order in Fig. 2.3 (right) has now been completely destroyed.

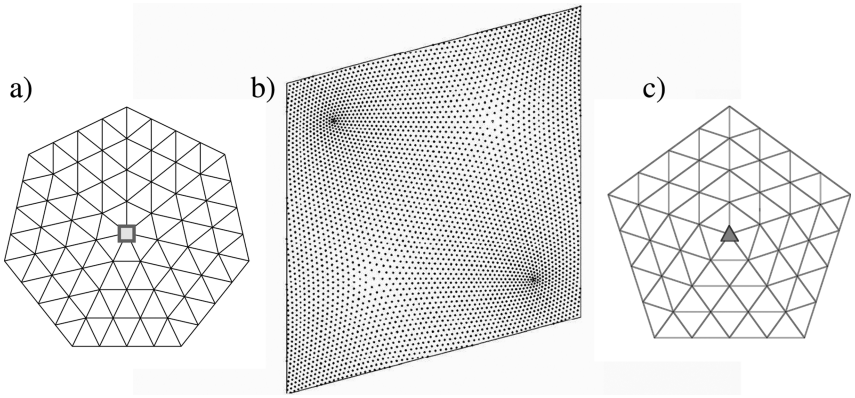

Fig. 2.6 (a) A $-\pi/3$ disclination in a triangular crystal with its sevenfold coordinated site in the center. (b) A system with four widely spaced disclinations (two $+\pi/3$ and two $-\pi/3$ disclinations). (c) A $+\pi/3$ disclination with its fivefold coordinated site.

In summary, we note that neither individual disclinations nor single dislocations can be produced through any kind of continuous transformation since they are topological defects. However, they can be produced via appropriately formed pairs: dislocations from $(5, 7, 5, 7)$ clusters, and disclinations from $(5, 7)$ dislocations. This natural production pathway suggests that with increasing temperature first dislocations and then disclinations will form in the crystal. The first defect type destroys the translational order [as we can predict from the inserted half line in Fig. 2.3 (right)] and transforms the crystal into what is known as the "hexatic phase", while occurrence of the second type of defect results in the destruction of the orientational order, leading to a phase transition into the fluid phase. We will elaborate on that further below.

2.2.2 Elastic Constants in Two-Dimensional Systems

In 2D hexagonal crystals there are only two independent elastic constants and the elastic free-energy density F can be written as

$$F = \tfrac{1}{2}\lambda u_{ii}u_{jj} + \mu u_{ij}u_{ij} \tag{2.3}$$

where $u_{ij} = (\partial_{x_i} u_j + \partial_{x_j} u_i)/2$ is the usual strain tensor derived from the displacement field with components u_i. Here we use the usual summation convention. In Eq. (2.3) λ and μ are called the Lamé coefficients. Decomposing u_{ij} into a scalar and a symmetric traceless tensor, we may rewrite Eq. (2.3) as

$$F = \tfrac{1}{2}Bu_{ii}^2 + \mu(u_{ij} - \tfrac{1}{2}\delta_{ij}u_{kk})^2 \tag{2.4}$$

with $B = \lambda + \mu$. The first term in this expression quantifies the elastic energy connected with pure area changes and, accordingly, B is called the bulk modulus. The second term corresponds to distortions in which the area of the crystal does not change, only its form, something that is characteristic of a pure shear deformation. Therefore, μ is termed the shear modulus. Equation (2.4) leads us to the stress tensor

$$\sigma_{ij} = \frac{\partial F}{\partial u_{ij}} = B u_{kk}\delta_{ij} + 2\mu(u_{ij} - \tfrac{1}{2}\delta_{ij}u_{kk}) \tag{2.5}$$

which can be inverted to give the strain in terms of the stress:

$$u_{ij} = \frac{1}{4B}\sigma_{kk}\delta_{ij} + \frac{1}{2\mu}(\sigma_{ij} - \tfrac{1}{2}\delta_{ij}\sigma_{kk}) \tag{2.6}$$

Now let us suppose that a 2D hexagonal crystal is subjected to a positive tension with a force per unit length T exerted across opposite sides, i.e. $f_y = T\,\mathrm{d}l$ is the force applied to the side of the crystal with normal in the $\vec{e}_y$ direction and $f_y = -T\,\mathrm{d}l$ is the force applied to the opposite side with normal $-\vec{e}_y$. Then $\sigma_{ij} = T\delta_{iy}\delta_{jy}$ and we obtain from Eq. (2.6)

$$u_{yy} = \left(\frac{1}{4B} + \frac{1}{4\mu}\right) T \tag{2.7}$$

$$u_{xx} = \left(\frac{1}{4B} - \frac{1}{4\mu}\right) T \tag{2.8}$$

$$u_{yx} = u_{xy} = 0$$

To cast this into a form similar to Hooke's law, we introduce a constant K such that Eq. (2.7) can be rewritten as $T = K u_{yy}$ with

$$K = \left(\frac{1}{4B} + \frac{1}{4\mu}\right)^{-1} = \frac{4B\mu}{B+\mu} = \frac{4\mu(\lambda+\mu)}{\lambda+2\mu} \tag{2.9}$$

This constant K is Young's modulus, which is nothing but the elastic constant that couples a uniaxial tension to the strain along the same direction. On the other hand, the strain along the normal direction determines what is known as Poisson's ratio, $\sigma = -u_{xx}/u_{yy}$. Hence, from Eqs. (2.7) and (2.8),

$$\sigma = \frac{B-\mu}{B+\mu} = \frac{\lambda}{\lambda+2\mu} \tag{2.10}$$

As we will see further below, for temperatures slightly above the melting temperature of the crystal, some order may remain even though the full translational symmetry has been destroyed. This residual order is an orientational one and characterizes the hexatic phase; it is described by a bond angle field $\theta(\vec{r})$ and controlled by a Hamiltonian of the form

$$H_A = \tfrac{1}{2}K_A(T)\int |\nabla\theta(\vec{r})|^2\,\mathrm{d}^2 r \tag{2.11}$$

with Frank's constant $K_A(T)$ as yet another elastic (scalar) constant relevant in the hexatic phase. In the fluid phase, finally, we have the compressibility as the only elastic constant.

2.2.3 Defects and Energies

We next calculate the energy for a single dislocation in a 2D crystal with triangular symmetry. To this end, we first need to know the displacement field $\vec{u}$ near the dislocation. In equilibrium the internal force $f_i = \partial_{x_j}\sigma_{ij}$ on each area element of the solid must be zero. Hence, from Eq. (2.5),

$$\lambda \frac{\partial u_{kk}}{\partial x_i} + 2\mu \frac{\partial u_{ij}}{\partial x_j} = 0 \tag{2.12}$$

for $i \in (x, y)$. As discussed in Section 2.2, a dislocation located at site $\vec{r}$ is characterized by the Burgers circuit, i.e. by the amount by which a contour integral of the displacement field taken around the dislocation fails to close,

$$\oint \mathrm{d}\vec{u} = a_0 \vec{b}(\vec{r}) \tag{2.13}$$

where $\vec{b}(\vec{r})$ is one of the three dimensionless Burgers vectors possible on a triangular lattice. The displacement field $\vec{u}$ is then a solution to the equilibrium equations (2.12), subject to the Burgers circuit constraint given in Eq. (2.13). For a dislocation $\vec{b} = b\vec{e}_x$ at the origin, the solution to this problem (Chaikin and Lubensky 1995; Nabarro 1967) reads

$$\begin{aligned} u_x &= \frac{ba_0}{2\pi}\left(\phi + \frac{K}{8\mu}\sin 2\phi\right) \\ u_y &= -\frac{ba_0}{2\pi}\left(\frac{\mu}{\lambda+2\mu}\ln r + \frac{K}{8\mu}\cos 2\phi\right) \end{aligned} \tag{2.14}$$

with (r, ϕ) being the usual cylindrical coordinates. One easily verifies that Eq. (2.13) is satisfied ($\int \mathrm{d}u_x = ba_0$ and $\int \mathrm{d}u_y = 0$). From this solution one can then obtain the associated stress tensor needed to eventually compute the energy of a dislocation,

$$E_{\mathrm{el}} = \tfrac{1}{2}\int \mathrm{d}^2 r\, \sigma_{ij} u_{ij} \tag{2.15}$$

resulting in

$$E = E_{\mathrm{el}} + E_{\mathrm{c}} = \frac{a_0^2 b^2 K}{8\pi}\ln\left(\frac{R}{a}\right) + E_{\mathrm{c}} \tag{2.16}$$

where we have restricted r to radii greater than a, the dislocation core radius, and smaller than R, the linear dimension of the sample. The calculation of the energy at the core of the defect would require some microscopic model

and is generally quite complicated. We therefore inserted some unspecified constant, the dislocation core energy E_c.

Repeating this calculation for two dislocations, $\vec{b}_1 = -\vec{b}_2 = \vec{b}$, a distance $\vec{r}_{12}$ apart from each other, we obtain

$$E = \frac{a_0^2 b^2 K}{4\pi} \ln\left(\frac{r_{12}}{a}\right) - \frac{a_0^2 K}{4\pi} \frac{(\vec{b}\cdot\vec{r}_{12})^2}{r_{12}^2} + 2E_c \tag{2.17}$$

We first note that the logarithmic divergence with system size of the expression in Eq. (2.16) disappears when two dislocations interact. This is due to the fact that we have considered a dislocation pair of antisymmetric Burgers vectors, which according to our considerations in Section 2.2 can be obtained by a continuous transformation starting from a regular lattice. Such a pair therefore cannot produce any kind of divergence with system size. More generally we may expect that there will be no $\ln R$ divergence in a system with many dislocations as long as $\sum_\alpha \vec{b}(\vec{r}_\alpha) = 0$. Secondly, we learn from Eq. (2.17) that two dislocations attract each other, obviously because this lowers the strain energy of the system. The second term in Eq. (2.17) is an angular term favoring a relative orientation of the two dislocations such that $\vec{r}_{12}$ becomes aligned to a vector perpendicular to $\vec{b}$.

Equation (2.17) can be generalized to an arbitrary distribution of dislocations at positions $\vec{r}_\alpha$,

$$H_D = -\frac{a_0^2 K}{4\pi}\frac{1}{2}\sum_{\alpha\neq\alpha'}\left[\vec{b}(\vec{r}_\alpha)\cdot\vec{b}(\vec{r}_{\alpha'})\ln\left(\frac{R_{\alpha,\alpha'}}{a}\right) - \frac{[\vec{b}(\vec{r}_\alpha)\cdot\vec{R}_{\alpha,\alpha'}]\,[\vec{b}(\vec{r}_{\alpha'})\cdot\vec{R}_{\alpha,\alpha'}]}{R_{\alpha,\alpha'}^2}\right] + E_c\sum_\alpha |\vec{b}(\vec{r}_\alpha)|^2 \tag{2.18}$$

with $\vec{R}_{\alpha,\alpha'} = \vec{r}_\alpha - \vec{r}_\alpha$. This Hamiltonian is called the "dislocation Hamiltonian" in the following. The neutrality of the dislocation gas is understood, i.e. $\sum_\alpha \vec{b}(\vec{r}_\alpha) = 0$. Note that, in principle, also triplets of appropriately chosen Burgers vectors can add up to zero and would thus be compatible with the neutrality condition. However, these so-called higher complexions are neglected in Eq. (2.18), which describes a gas of only pairwise interacting dislocations. Note also that $\sum_\alpha |\vec{b}(\vec{r}_\alpha)|^2$ is just the number of dislocations in the system.

Equation (2.18) is still not the most general case possible. At sufficiently high temperatures, both disclinations and dislocations are present in the system, and each type interacts not only with its own class of defects but also with the other defect class. So, we consider an arbitrary distribution of dislocations and disclinations. As discussed in Section 2.2, a disclination is characterized by the angles through which the two sides of the Volterra cut can

be rotated. In a hexagonal lattice, these are the angles $\pm\pi/3$. A distribution of disclinations is now best represented by a disclination density

$$s(\vec{r}) = \sum_\alpha s_\alpha \delta(\vec{r} - \vec{r}_\alpha) \tag{2.19}$$

where $s_\alpha = \pm 1$, while a distribution of dislocations is described by a vector dislocation density

$$\vec{b}(\vec{r}) = \sum_\alpha \vec{b}_\alpha \delta(\vec{r} - \vec{r}_\alpha) \tag{2.20}$$

with the Burgers vectors $\vec{b}_\alpha$ for dislocations at positions $\vec{r}_\alpha$. The Fourier transforms of these quantities are

$$\begin{aligned} s(\vec{q}) &= \sum_\alpha s_\alpha \mathrm{e}^{-\mathrm{i}\vec{q}\vec{r}_\alpha} \\ \vec{b}(\vec{q}) &= \sum_\alpha \vec{b}_\alpha \mathrm{e}^{-\mathrm{i}\vec{q}\vec{r}_\alpha} \end{aligned} \tag{2.21}$$

We can now define a total defect density by adding the disclination density (which can be considered as "free" disclinations) and a contribution stemming from the dislocations (which can be considered as "bound" disclinations),

$$\tilde{s}(\vec{q}) = \tfrac{1}{3}\pi s(\vec{q}) + \mathrm{i}a_0[q_y b_x(\vec{q}) - q_x b_y(\vec{q})] \tag{2.22}$$

Note that now $\pi/3$ and a_0 are to be inserted since both defect variables s_α and $\vec{b}_\alpha$ are chosen such that their modulus is unity. The generalization of Eq. (2.13) now reads

$$\oint_\Gamma \mathrm{d}u_i = a_0 \sum_\alpha b_{\alpha j} \qquad \oint_\Gamma \mathrm{d}\theta = \tfrac{1}{3}\pi \sum_\alpha s_\alpha \tag{2.23}$$

where the sum is over all $\vec{b}_\alpha$ and s_α enclosed by Γ. The energy associated with this general defect distribution can be calculated once the strain and stress field is obtained from solving Eq. (2.12) together with (2.23). One finds (Chaikin and Lubensky 1995)

$$H_{\mathrm{DD}} = \tfrac{1}{2}K \int \frac{\mathrm{d}^2 q}{(2\pi)^2} \frac{1}{q^4} \tilde{s}(\vec{q})\tilde{s}(-\vec{q}) + E_\mathrm{c} \sum_\alpha b_\alpha^2 + E_\mathrm{s} \sum_\alpha s_\alpha^2 \tag{2.24}$$

as the Hamiltonian of a mixed system of dislocations and disclinations. Here E_s is the disclination core energy. From this expression Eq. (2.16) is recovered if $s(\vec{r})$ is set to zero and just one Burgers vector is assumed to be placed at the origin. In addition, the dislocation Hamiltonian in Eq. (2.18) is reproduced by setting $s(\vec{r}) = 0$. On the other hand, setting $\vec{b}(\vec{r}) = 0$ in Eqs. (2.20) and (2.22), and considering just one single disclination at the origin, one obtains an R^2 divergence with the system size R, which again, as in the case of dislocations, disappears if two oppositely charged disclinations are considered.

In the hexatic phase, i.e. the phase intervening between the crystal and the isotropic phase, free disclinations become energetically possible. The interaction between these disclinations is screened by the dislocations. Applying the Debye–Hückel approximation, it is now possible to integrate out the dislocation degrees of freedom in Eq. (2.24), and to replace Eq. (2.24) by a pure disclination Hamiltonian but with effective disclination–disclination interactions (Chaikin and Lubensky 1995; Nelson and Halperin 1979). One obtains

$$H_{\mathrm{disc}} = K_A \left(\frac{\pi}{3}\right)^2 \int \frac{\mathrm{d}^2 q}{(2\pi)^2} \frac{1}{q^2} s(\vec{q}) s(-\vec{q}) + E_{\mathrm{s}} \sum_{\alpha} s_\alpha^2 \tag{2.25}$$

with the coupling constant

$$K_A = \frac{2E_{\mathrm{c}} a^2}{a_0^2} \tag{2.26}$$

The appearance of the dislocation core energy and radius in this constant – which can be interpreted as a Frank constant – is all that remains of the dislocation degrees of freedom. Equation (2.25) in direct space reads

$$H_{\mathrm{disc}} = -\frac{K_A}{2\pi} \left(\frac{\pi}{3}\right)^2 \frac{1}{2} \sum_{\alpha \neq \alpha'} s_\alpha s_{\alpha'} \ln\left(\frac{R_{\alpha,\alpha'}}{a_{\mathrm{s}}}\right) + E_{\mathrm{s}} \sum_{\alpha} s_\alpha^2 \tag{2.27}$$

where $\vec{R}_{\alpha,\alpha'} = \vec{r}_\alpha - \vec{r}_\alpha$ and a_{s} is the disclination core radius. So, neglecting for a moment the angular term in Eq. (2.17), we may summarize this section by observing that both a dislocation pair ($\vec{b}_1 = -\vec{b}_2$) and a disclination pair ($s_1 = -s_2$) attract each other via a pair potential of the form

$$\beta v(r) = c \ln(r/a) \tag{2.28}$$

($\beta = 1/k_{\mathrm{B}}T$) where

$$c = \frac{\beta K a_0^2}{4\pi} \qquad \text{for a dislocation pair} \tag{2.29}$$

$$c = \frac{\beta K_A \pi}{18} \qquad \text{for a disclination pair} \tag{2.30}$$

The pair potential (2.28) is used in the next section to estimate the mean distance between defect pairs.

2.2.4 Melting in Two Stages

As already mentioned at the end of Section 2.2 the key idea of the KTHNY melting theory is that the unbinding of defect pairs is responsible for the melting. More specifically, the unbinding of dislocation pairs produces a first transition at T_{m}, and the subsequent unbinding of dislocations into disclinations produces a second transition at a somewhat higher temperature T_{i}.

The presence of free dislocations in the system is not compatible with the translational symmetry. So, at temperatures $T_\mathrm{i} > T > T_\mathrm{m}$ where free dislocations (but not yet free disclinations) can exist, the crystalline order is destroyed. The system has undergone a phase transition from solid to another phase, the hexatic phase. This phase is characterized by an algebraic decay of the orientational order parameter but an exponential short-range decay of the translational order parameter. Then for $T > T_\mathrm{i}$ free disclinations can occur which now destroy the residual orientational order. The system has entered into the isotropic fluid phase in which we have an exponential decay of both orientational and translational order parameter.

On the basis of this qualitative picture we can now estimate the two temperatures T_m and T_i using the defect pair interaction Hamiltonian in Eq. (2.28) to calculate the mean quadratic distance between defect pairs,

$$\langle r^2 \rangle = \frac{\int \mathrm{d}^2 r \, r^2 \mathrm{e}^{-\beta v(r)}}{\int \mathrm{d}^2 r \, \mathrm{e}^{-\beta v(r)}} = \frac{2-c}{4-c} \, a^2 \tag{2.31}$$

where we have had to assume that $c > 4$. For $c \to 4$, the expression diverges, $\langle r^2 \rangle \to \infty$, meaning that the defect pair dissociates. Hence, the dislocation unbinding temperature for a dislocation pair results from

$$\frac{\beta K a_0^2}{4\pi} \to 4 \tag{2.32}$$

or, equivalently,

$$k_\mathrm{B} T_\mathrm{m} = \frac{K a_0^2}{16\pi} \tag{2.33}$$

where we used Eq. (2.29). The unbinding temperature for a disclination pair follows from Eqs. (2.31) and (2.30),

$$\frac{\beta K_A \pi}{18} \to 4 \tag{2.34}$$

or

$$k_\mathrm{B} T_\mathrm{i} = \frac{K_A \pi}{72} \tag{2.35}$$

In other words, from Eq. (2.32),

$$\lim_{T \to T_\mathrm{m}^-} \frac{K(T) a_0^2}{k_\mathrm{B} T} = 16\pi \tag{2.36}$$

and from Eq. (2.34),

$$\lim_{T \to T_\mathrm{i}^-} \frac{K_A(T)}{k_\mathrm{B} T} = \frac{72}{\pi} \tag{2.37}$$

where the negative sign as the superscript index of T_m and T_i serves as a reminder of the fact that both limits are approached from below, reflecting the pair stability condition $c > 4$. Both equations link a transition temperature to those elastic constants which are characteristic of the phases involved. These

equations define the point where microscopic details of the defect interaction are transformed into a prediction based purely on macroscopic information; they are important predictions of the KTHNY theory as their derivation is based on the essential KTHNY idea of defect unbinding. Equation (2.37) should be seen in connection with Eq. (2.26), and is correct as it stands. Equation (2.36), however, needs a further modification discussed in the next section.

2.2.5
The Halperin–Nelson Recursion Relations

The physical picture underlying Eq. (2.36) is that on approaching T_{m} the crystal softens until $K(T)/T$ is small enough to allow dislocations to unbind. The crystal melts. The temperature dependence of $K(T)$ can result partly from higher anharmonic terms in the crystal phonon Hamiltonian, an effect that is called "thermal softening" [see Section 7.7 in Kleinert (1989)]. However, the elastic constants can also and additionally be softened by dislocations. So, the role of the Young's modulus here is twofold: it determines the dislocation unbinding, but is itself influenced by the system of interacting dislocations. This very fact suggests that recursion relations are needed to obtain the elastic constants in the presence of a gas of interacting dislocations.

These recursion relations have been derived by Nelson and Halperin (1979). These authors decompose the strain tensor into a smoothly varying part $\phi_{ij}(\vec{r})$ for the perfect crystal and a singular part $u_{ij}^{\mathrm{sing}}(\vec{r})$ which is due to the dislocations, and they write the full system Hamiltonian H as a sum of Eqs. (2.3) and (2.18),

$$H = H_0 + H_{\mathrm{D}} = \tfrac{1}{2} \int \mathrm{d}^2 r \, (\lambda \phi_{ii}^2 + 2\mu \phi_{ij} \phi_{ij}) + H_{\mathrm{D}} \tag{2.38}$$

where the perfect crystal part H_0 resorts just to $\phi_{ij}(\vec{r})$. For a system that is thought to be defect-free, $H_0(\lambda, \mu)$ depends on λ and μ. The idea now is to renormalize both constants $\lambda \to \lambda_{\mathrm{R}}$ and $\mu \to \mu_{\mathrm{R}}$ such that $H_0(\lambda, \mu) + H_{\mathrm{D}}$ can be replaced by a single Hamiltonian $H_0(\lambda_{\mathrm{R}}, \mu_{\mathrm{R}})$ for an ersatz system without dislocations but with somewhat softer elastic constants. The effect of the dislocations is thus absorbed into the elastic constants. This defect-mediated softening adds to the thermal softening.

Of crucial importance in this theory is the dislocation core energy E_{c}, appearing in the last term of Eq. (2.18), or, more precisely, the quantity $y = \mathrm{e}^{-E_{\mathrm{c}}/k_{\mathrm{B}}T}$. To quadratic order in y and for a triangular lattice, Halperin and Nelson (1978) derived coupled differential equations for $K(l)$, $\mu(l)$, $\lambda(l)$ and $y(l)$, all four quantities expressed as a function of the renormalization flow variable l. The value $l = 0$ corresponds to the unrenormalized values,

$l \to \infty$ to the renormalized ones. Here we repeat only the renormalization group equations for $K(l)$ and $y(l)$,

$$\begin{aligned} \frac{\mathrm{d}K^{-1}(l)}{\mathrm{d}l} &= \frac{3}{2}\pi y^2 \mathrm{e}^{K(l)/8\pi} I_0\left(\frac{K(l)}{8\pi}\right) - \frac{3}{4}\pi y^2 \mathrm{e}^{K(l)/8\pi} I_1\left(\frac{K(l)}{8\pi}\right) \\ \frac{\mathrm{d}y(l)}{\mathrm{d}l} &= \left(2 - \frac{K}{8\pi}\right) y(l) + 2\pi y^2 \mathrm{e}^{K(l)/16\pi} I_0\left(\frac{K(l)}{8\pi}\right) \end{aligned} \tag{2.39}$$

where I_0 and I_1 are modified Bessel functions. Let us discuss the solutions to these differential equations considering a special 2D system which can be realized by colloidal particles and which will be properly presented and discussed in the next sections. We consider a 2D system of particles interacting with a pair potential of the form $\beta v(r) = \Gamma/(r/d_{\mathrm{nn}})^3$ [see Eq. (2.58)] where d_{nn} is the nearest-neighbor distance and Γ is the interaction strength parameter, inversely proportional to the temperature T. For $T \to 0$ the Young's modulus for this system can be calculated (Zanghellini et al. 2005) yielding

$$\beta a_0^2 K = 1.258\Gamma \tag{2.40}$$

Assuming this value for K and furthermore a core energy of $E_{\mathrm{c}} = 5.4 k_{\mathrm{B}} T$ as the $l = 0$ values we can now solve Eq. (2.39) numerically, for a number of different temperatures as done in Fig. 2.7 (a). We observe that for low temperatures, i.e. if $\Gamma > 60$, y vanishes for $l \to \infty$, and we obtain $1/K_{\mathrm{R}} = 1/K(\infty)$, which is always higher than $1/K(0)$. This means that the crystal in our ersatz system has no defects but is somewhat softer since $K_{\mathrm{R}} < K(0)$. For $\Gamma < 60$, the fugacity no longer vanishes and renormalization becomes impossible. This marks the point where the crystal is no longer stable against free dislocations – it melts. Analyzing Eq. (2.39) one can show that the so-called separatrix (line separating the stable from the unstable solutions) will always terminate at $a_0^2 \beta K_{\mathrm{R}} = 16\pi$; see Fig. 2.7 (a).

With this latter result we can come back to Eq. (2.36). The unbinding temperature for two dislocations in the presence of a gas of interacting dislocations is quantified by Eq. (2.36) but with K replaced by K_{R},

$$\lim_{T \to T_{\mathrm{m}}^-} \frac{K_{\mathrm{R}}(T) a_0^2}{k_{\mathrm{B}} T} = 16\pi \tag{2.41}$$

This is a universal relationship which should be true for all 2D systems that show a defect-mediated melting, no matter what form of interaction they are characterized by. The same result is obtained by balancing the energy and entropy of an isolated dislocation as was done by Kosterlitz (1974). Equation (2.41) is therefore called the Kosterlitz–Thouless criterion for melting. Since we can expect the Lamé coefficient μ to be zero above T_{m}, $K_{\mathrm{R}}(T)$ should be discontinuous at the melting temperature.

Figure 2.7 (a) provides us with K_{R} versus Γ. However, we have to take account of thermal softening as well. Figure 2.7 (b) shows the Young's mod-

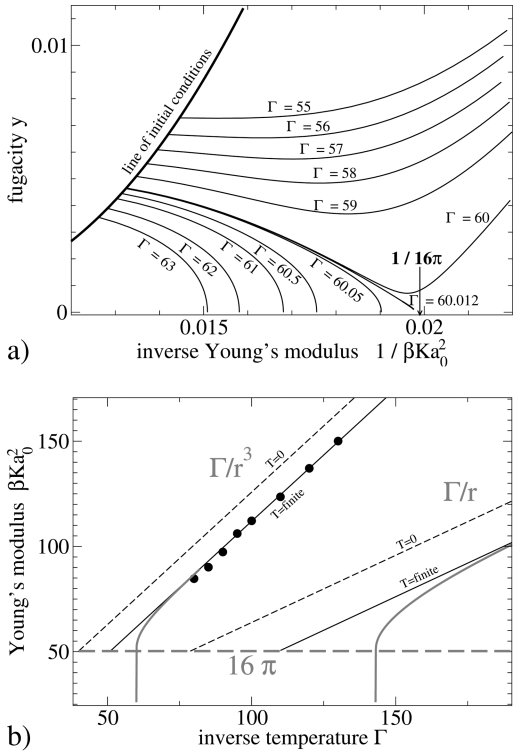

Fig. 2.7 (a) Solutions to the Halperin–Nelson renormalization group equations in Eq. (2.39) for a 2D system with $1/r^3$ pair interactions. Γ can be considered as inverse temperature. Each line corresponds to one temperature and shows $(y(l), K^{-1}(l))$ as a function of l starting from $(y(0), K^{-1}(0))$. For temperatures where $y(l)$ vanishes in the limit $l \to \infty$, the crystal is stable against dislocation unbinding, while it is unstable for temperatures where $y(l) \to \infty$ for $l \to \infty$. The melting temperature (here $\Gamma \approx 60$) belongs to the line separating both regimes (the "separatrix").
(b) Young's modulus as a function of Γ for a system with $1/r^3$ and $1/r$ pair interactions. In both systems Young's modulus has been approximated using elastic constants from (i) zero-temperature calculation (dashed line), (ii) finite-temperature simulation (thin solid line), and (iii) integrating the KTHNY equations (2.39) (thick solid line). The difference between the curves (i) and (ii) shows the effect of thermal softening, while the difference between the curves (ii) and (iii) is produced by a defect-mediated softening. Simulation data for $1/r^3$ are marked with filled circles.

ulus for a warm and defect-free crystal with pair interaction $1/r^3$ as obtained from Monte Carlo simulations (Zanghellini et al. 2005) (thin solid line). The results for finite temperature are markedly different from the $T = 0$ approximation (2.40) used above. Taking these finite-temperature results as initial conditions for solving Eq. (2.39) (and assuming $E_c = 5.7 k_B T$), one obtains $K_R(\Gamma)$ with the correct low-temperature behavior (thick solid line in Fig. 2.7

b). It passes through 16π at $\Gamma = 60$. Note the considerable extra softening produced by the defects near the unbinding temperature (difference between thick solid and thin solid lines). Figure 2.7 (bottom) also shows the corresponding results for a system with $1/r$ interactions as realized for instance by electrons on liquid helium.

We observe that a similar renormalization procedure for the Frank constant in Eq. (2.37) is not needed. Here it is not the other disclinations but the dislocations that are assumed to affect the Frank constant, and their screening effect is already taken into account in going from Eq. (2.24) to the effective Hamiltonian in (2.25), with the effect that K_A is given by Eq. (2.26). We should finally also remark that the Frank constant should be discontinuous at T_i, just as $K_\mathrm{R}(T)$ is for $T > T_\mathrm{m}$.

2.2.6 Correlation Functions

The Translational Order

Let us now consider the order in the *crystalline phase*, i.e. for $T < T_\mathrm{m}$. Crystals in 2D systems are well studied, mainly in the context of problems in surface science. Many monolayers are approximate realizations of systems in mathematical two dimensions – see Sections 4.2 and 4.3 in Bruch et al. (1997). Perhaps the most spectacular feature of 2D crystals is the fact that the mean square displacement $\langle|\vec{u}(\vec{R})|^2\rangle$ diverges, with $\vec{u}(\vec{R})$ being the displacement of a particle from its lattice site $\vec{R}$. It is therefore more fruitful to study the mean square relative displacement

$$W_{ij} = \langle \Delta u_i(\vec{R}) \Delta u_j(\vec{R}) \rangle \tag{2.42}$$

with $\Delta u_i(\vec{R}) = u_i(\vec{R}) - u_i(\vec{0})$. For large separations R the asymptotic evaluation of this quantity gives the simple expression (Nelson and Halperin 1979; Bruch et al. 1997)

$$W_{ij} = \eta a_0^2 \delta_{ij} \ln\left(\frac{R}{a}\right) \tag{2.43}$$

with

$$\eta = \frac{k_\mathrm{B}T}{\pi \mu_R a_0^2} \frac{3\mu_\mathrm{R} + \lambda_\mathrm{R}}{2\mu_\mathrm{R} + \lambda_\mathrm{R}} \tag{2.44}$$

The logarithmic divergence with R in Eq. (2.43) is typical of 2D crystals, and is not found in 3D crystals. With Eq. (2.43), one can now estimate the Debye–Waller correlation function $C_{\vec{q}}(\vec{R})$ appearing in the structure factor

$$S(\vec{q}) = \sum_{\vec{R}} \mathrm{e}^{\mathrm{i}\vec{q}\vec{R}} C_{\vec{q}}(\vec{R}) \tag{2.45}$$

which is approximately given by

$$C_{\vec{q}}(\vec{R}) \approx \mathrm{e}^{-\frac{1}{2} q_i q_j W_{ij}} \tag{2.46}$$

Inserting Eq. (2.43) into this equation yields

$$C_{\vec{q}}(\vec{R}) \approx \left(\frac{a}{R}\right)^{q^2 a_0^2 \eta/2} \tag{2.47}$$

In 3D crystals $S(\vec{q})$ has a set of δ-function Bragg peaks, occurring at the reciprocal lattice vectors $\vec{G}$, and due to the finiteness of $\vec{u}(\vec{R})$ the Debye–Waller function $C_{\vec{G}}(\vec{R})$ tends to non-zero constants at large $\vec{R}$. This is not so in 2D. Here, $\vec{u}(\vec{R})$ is not finite and $C_{\vec{G}}(\vec{R})$ tends algebraically to zero for large R like $\sim R^{-\eta_G}$ with an exponent $\eta_G = \eta G^2 a_0^2/2$. Also the δ-functions of the Bragg peaks in 3D crystals are in 2D crystals replaced by power-law singularities $\sim |\vec{q} - \vec{G}|^{-2+\eta_G}$.

The Debye–Waller function $C_{\vec{G}}(\vec{R})$ can be related to the envelope function of the pair distribution function

$$g(r) = \frac{V}{N^2} \left\langle \sum_{i,\, j \neq i} \delta(\vec{r} - \vec{r}_{ij}) \right\rangle \tag{2.48}$$

and is thus easy to observe also in real space.

For $T > T_{\mathrm{m}}$ one observes a different decay behavior. Here $C_{\vec{G}}(\vec{R})$ decays exponentially $\sim \mathrm{e}^{-R/\xi}$. We note that one can get access to the important elastic constants via η from Eq. (2.44) either by analyzing the mean square relative displacement in Eq. (2.42) or, alternatively, by studying the decay behavior of $C_{\vec{G}}(\vec{R})$ [by analyzing $g(r)$ or $S(q)$]. For $T \to T_{\mathrm{m}}^-$ the index η also goes to a universal value [just like the Young's modulus in Eq. (2.36)] and can in principle also be used to check the KTHNY melting scenario [see Zanghellini et al. (2005)].

In summary, the decay of $C_{\vec{G}}(\vec{R})$ to zero is a signature of the fact that there is now true translational order in 2D crystals. Nevertheless, it is just a slow power-law decay which is markedly different from the exponential decay one finds for $T > T_{\mathrm{m}}$. This allows us to speak of a quasi-long-range order and still to distinguish the crystalline from the two other phases.

The Orientational Order

The bond orientational order in triangular lattices is usually quantified using the following orientational correlation function:

$$g_6(r) = \langle \psi_6(\vec{r}) \psi_6^*(\vec{0}) \rangle \tag{2.49}$$

with

$$\psi_6(\vec{r}_l) = \frac{1}{n_l} \sum_{j=1}^{n_l} \mathrm{e}^{i 6 \theta_{lj}(\vec{r}_l)} \tag{2.50}$$

where n_l is the number of neighbors of the particle at $\vec{r}_l$ and $\theta_{lj}(\vec{r}_l)$ is the orientation relative to some fixed reference axis of the bond between a particle

at $\vec{r}_l$ and $\vec{r}_j$ (Fig. 2.8). In the crystalline phase this function is a constant (Nelson and Halperin 1979),

$$\ln g_6 = -\frac{9}{8\pi}\frac{k_\mathrm{B}T}{\mu_\mathrm{R}a_0^2} \tag{2.51}$$

which in a real-space experiment is easy to measure and provides access to the shear modulus. Now, in the hexatic phase, i.e. above T_m but below the second transition temperature T_i, g_6 shows an algebraic decay behavior $\sim r^{-\eta_6}$ with an exponent

$$\eta_6 = \frac{18k_\mathrm{B}T}{\pi K_A} \tag{2.52}$$

which is related to the Frank constant, Eq. (2.26). Recalling Eq. (2.37), we observe that

$$\lim_{T\to T_\mathrm{i}^-}\eta_6 \to \frac{1}{4} \tag{2.53}$$

Finally, at $T > T_\mathrm{i}$ the orientational order decays again exponentially $\sim \mathrm{e}^{-r/\xi_6}$ with a correlation length ξ_6 that goes like $\ln\xi_6 \sim |T - T_\mathrm{i}|^{-1/2}$ for $T \to T_\mathrm{i}^+$. We have already remarked in the discussion of Eq. (2.37) that K_A jumps discontinuously to zero at T_i, implying that η_6 here jumps to infinity so that the algebraic decay of g_6 comes to a natural end at T_i.

2.3 Experiments in Two Dimensions

In the following we list a few 2D experiments that have been designed to study phase transitions in 2D and, in particular, to check the predictions of the KTHNY theory. While this section focusses more on the experimental techniques, the next section will be devoted to a discussion of the results and their implications regarding the theory of melting.

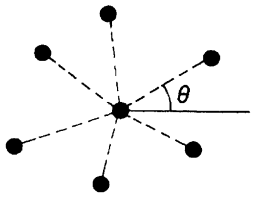

Fig. 2.8 "Bonds" (dashed lines) joining a central particle to its six neighbors. Each bond makes an angle θ with a fixed reference axis.

2.3.1 Systems Not Involving Colloids

As outlined in the Introduction, 2D colloidal systems are the focus of this chapter, but there are numerous other appropriate systems to study 2D melting. The following list of them is far from being complete and is intended more to demonstrate the rich variety of 2D systems with which different parts of the KTHNY theory have been tested. Grimes and Adams (1979) were the first to study the transition from a 2D fluid phase to a 2D crystal of electrons ("Wigner" crystal) on the surface of fluid helium by measuring microwave absorption. Since these measurements are not sensitive to the orientational correlation, the existence of the hexatic phase could not be demonstrated. Dimon et al. (1985) and Heiney et al. (1982) investigated a monolayer of xenon atoms on graphite and found some evidence for the hexatic phase from X-ray scattering data, but were not able to control the effect of the periodic substrate on the phase behavior. By comparison with simulations Li and Rice (2005) showed that the out-of-plane motion of a monolayer of Pb atoms on a PbGa alloy liquid–vapor interface suppresses the hexatic phase. Free-standing liquid-crystal films showed short-range translational and long-range orientational order (Pindak et al. 1981; Davey et al. 1984), but such films consist of a few molecular layers and are therefore certainly not purely 2D. Detailed studies of the temperature dependence of the correlation length in thin block copolymer films have been reported by Segalman et al. (2003). In Angelescu et al. (2005) a first-order melting transition was observed in a similar system, but the role of the finite film thickness and the coupling to substrate inhomogeneities remained unclear. Indications of a hexatic structure were also found in a stationary non-equilibrium system of magnetic bubble arrays driven by an AC magnetic field (Seshadri and Westervelt 1992) and in thin layers of granular systems where thermal motion was induced by mechanical vibrations (Reis et al. 2006; Zheng and Grieve 2006). Some evidence for two-step melting was seen in layers of millimeter-sized particles which were levitated against gravity by vertical electric-field-driven currents in dense dusty plasma (Melzer et al. 1996; Quinn and Goree 2001). The use of the latter systems as model systems for 2D melting is not evident given the fact that they are driven far out of thermodynamic equilibrium.

2.3.2 Colloidal Systems with Screened Coulomb Interaction

We next turn to 2D systems built out of micrometer-sized colloidal particles. They have many advantages compared to the systems mentioned above. The most important advantage of using colloidal particles is that they are big enough to be directly observable by means of video-microscopy. At the same

time they are still small enough to perform thermally driven ("Brownian") motion and can thus be considered as a statistical ensemble in thermal equilibrium. Not only the length scale but also the time scale for configuration changes are in an easily observable regime, since it takes typically seconds for them to diffuse across their own diameter. Using digital image processing the trajectories of the particles can be extracted and analyzed numerically on all relevant time and length scales.

In Murray and Van Winkle (1987) and Tang et al. (1989) charged spherical colloids (polystyrene-sulfonate microspheres) were used in aqueous suspension. Confinement to two dimensions was realized by squeezing the suspension between two nearly parallel glass plates providing a thin film. The colloids strongly ionize [typically 20 000 e^- for particles with 0.3 μm diameter (Murray and Van Winkle 1987)] and the colloid–colloid pair interaction is a screened Coulomb potential where the screening is ultimately due to the counterions in the solution. Murray et al. were the first to identify the hexatic phase in colloidal systems by measuring the structure factors of this system, which were similar to those given in Fig. 2.2. In addition they determined the distance dependence of the orientational correlation function in Eq. (2.49). They used a wedge geometry of the glass plates so that the thickness of the fluid layer increased from 1 ± 0.3 μm with an inclination of $4 \pm 0.5 \times 10^{-4}$ rad in one direction. Due to the additional interaction of the colloids with the glass plates, a density gradient of the particles appeared in equilibrium with low density in the thin-film region. Because of this, different types of crystal symmetries were found in the arrangement of the colloids along the density gradient. In the high-density region, 2000 particles were observable in the field of view of $38 \times 25\,\mu m^2$; while in the low-density region, only about 100 particles were traced.

In order to avoid a possible influence of the inherent particle density gradient, a flat cell geometry was used by Tang et al. (1989). Two disk-shaped glass plates with different diameters were glued concentrically on top of each other, so that the smaller one would act like a stamp when pressed against a third plate. The space between the first and third glass plates was sealed by a rubber O ring near the circumference. The ring-like space between the small plate and the O ring was used as a 3D reservoir for the $1\,\mu m$-sized spheres. Reducing the gap between plates two and three below $\sim 5\,\mu m$, the 2D population of colloids expanded into the reservoir. In this way a crystal of 3430 particles was molten over 7 h to a liquid with 1460 particles in the field of view of $277 \times 222\,\mu m^2$. A faster melting rate did not seem to change the results. The hexatic phase was observed but the possibility of the coexistence of the isotropic liquid and the hexatic phase could not be ruled out.

2.3.3
Colloidal Systems with Hard-Core Repulsion

Marcus and Rice (1996) [see also Marcus and Rice (1997)] set up a colloidal system with essentially hard-core repulsion combined with a short-range square attractive part. They used polymethylmethacrylate microspheres sterically stabilized against van der Waals attraction with a layer of poly(12-hydroxystearic) acid. Particles of diameter $0.93\,\mu\mathrm{m}$ were suspended in aqueous sucrose solution (10% by weight) in order to eliminate sedimentation. The spacing between the walls of a flat thin glass cell was found to be optimal at $\sim 1.2\,\mu\mathrm{m}$, thereby avoiding immobilization at lower and out-of-plane motion at higher distances. The quantity to be varied in different measurements was the particle density. Marcus and Rice clearly demonstrated the existence of a hexatic phase and observed isotropic–hexatic and hexatic–crystal phase equilibria at both transitions. Again the influence of the confining walls remained unclear. Studying a colloidal system with perfect hard-core interaction, Karnchanaphanurach et al. (2000) were not able to identify a hexatic phase.

2.3.4
Colloidal Systems with Dipole Interaction

The first 2D melting study using induced dipole interaction was published by Kusner et al. (1994). These authors introduced the idea that the effective system temperature can be varied in situ at constant particle densities by controlling their induced dipole moment through an external field (Kusner et al. 1995).

Polystyrene particles of $1.6\,\mu\mathrm{m}$ diameter in aqueous solution were confined between parallel glass plates of $2.4\,\mu\mathrm{m}$ spacing. The colloids were sulfonated with a concentration of $2\times10^{13}\ \mathrm{SO}_4^-$ surface groups. The glass plates were covered with a 20 nm Au film serving as transparent electrodes for the electric field which polarizes the colloids and induces an electric dipole–dipole interparticle potential. The electric field had a frequency of 3.75 MHz in order to prevent screening by counterions. If water and polymer particles are treated as isolating dielectrics, the pair potential is given by

$$U(r) = \frac{\epsilon_\mathrm{w}(\epsilon_\mathrm{w}-\epsilon_\mathrm{s})^2}{(2\epsilon_\mathrm{w}+\epsilon_\mathrm{s})^2}\frac{r_\mathrm{s}^6}{r^3}\langle|\vec{E}_\mathrm{w}|^2\rangle \tag{2.54}$$

where ϵ_w and ϵ_s are the dielectric constants of water and colloid, respectively, r_s is the radius of the sphere, and $\vec{E}_\mathrm{w}$ is the electric field. The phase behavior depends on the ratio of the potential versus the thermal energy described with the dimensionless interaction strength Γ defined as

$$\Gamma = \frac{U(r_\mathrm{WS})}{k_\mathrm{B}T} \propto \frac{1}{T_\mathrm{sys}} \tag{2.55}$$

where $r_{\mathrm{WS}} = 1/\sqrt{\pi\rho}$ is the Wigner–Seitz radius, with ρ being the 2D density. Γ can be interpreted as an inverse temperature and is externally controlled by means of the electric field $\vec{E}_{\mathrm{w}}$. The interaction strength is the only parameter controlling the phase behavior of the system. At high Γ the sample is a hexagonal crystal, whereas for low Γ it is an isotropic fluid. Exploiting $g_6(r)$ data and taking screening of counterions into account, Kusner et al. found a hexatic to crystalline transition at $\Gamma_{\mathrm{m}} = 60 \pm 3$.

The key problem in the 2D colloidal systems discussed above is the confinement between glass plates. First, the neighborhood of the plates implies that the screening length of the Yukawa potential due to counterions in the presence of the glass surfaces is ill defined and may evolve in time over the experiment. In addition, surface roughness or impurities at the plates may lead to pinning centers for the colloidal particles. We next describe in detail the 2D system of superparamagnetic colloids at the free air–water interface which circumvents these problems. It was originally developed by Zahn (1997) [see also Zahn et al. (1997), Zahn et al. (1999), and Zahn and Maret (2000)] and later improved by Keim (2005).

The experimental setup consists of spherical colloids (diameter $d = 4.5\,\mu\mathrm{m}$) that are confined by gravity to a water–air interface formed by a water drop suspended by surface tension in a top-sealed cylindrical 8 mm diameter hole of a glass plate (see Figs. 2.9 and 2.10). Due to Fe_2O_3 doping the particles are superparamagnetic and rather heavy, with a mass density $\approx 1.5 \times 10^{-3}\,\mathrm{kg\,m^{-3}}$ and a susceptibility per particle $\chi = 6.47 \times 10^{-11}\,\mathrm{A\,m^2\,T^{-1}}$ obtained by SQUID measurements. A magnetic field $\vec{H}$ applied perpendicular to the air–water interface induces a magnetic moment $\vec{M} = \chi\vec{H}$ in each particle, which leads to the repulsive dipole–dipole pair interaction

$$E_{\mathrm{magn}} = \frac{\mu_0}{8\pi}\frac{m^2}{r^3} = \frac{\mu_0}{4\pi}\frac{\chi^2\vec{H}^2}{r^3} \tag{2.56}$$

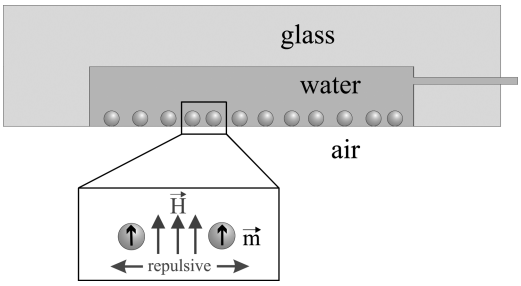

Fig. 2.9 Superparamagnetic colloids confined at a water–air interface due to gravity (side view). A magnetic field $\vec{H}$ perpendicular to the interface induces a magnetic moment $\vec{m}$ leading to a repulsive interaction.

with χ being the susceptibility per colloid. The interaction strength Γ is then defined by E_{magn} at the nearest-neighbor distance $d_{\mathrm{nn}} = (\pi\rho)^{-1/2}$,

$$\Gamma = \frac{E_{\mathrm{magn}}}{k_{\mathrm{B}}T} = \frac{\mu_0}{4\pi}\frac{\chi^2\vec{H}^2(\pi\rho)^{3/2}}{k_{\mathrm{B}}T} \propto \frac{1}{T_{\mathrm{sys}}} \tag{2.57}$$

so that the particle–particle interaction becomes

$$\beta v(r) = \frac{\Gamma}{(r/d_{\mathrm{nn}})^3} \tag{2.58}$$

The ensemble of particles is visualized with video-microscopy from above and the signal of a CCD 8-bit gray-scale camera is analyzed on a computer. The field of view has a size of $835 \times 620\,\mu\mathrm{m}^2$ containing typically up to 3×10^3 particles, whereas the whole sample contains up to about 3×10^5 particles. In order to get size, number, and positions of the colloids, the image is binarized: all pixels with a gray level above a suitable cutoff are set to white whereas pixels below the cutoff are set to black. The software recognizes areas of connected pixels (called blobs) with respect to the uniform background; the amount of connected pixels of each blob gives the projected size of the colloid and the barycenter gives its position. The average projected size of the colloids gives information about the vertical position of the interface relative to the focus of the camera. If the camera is moved in the vertical direction, particle images are smallest in focus and bigger out of focus (see Fig. 2.10). This information is used to maintain a flat water surface

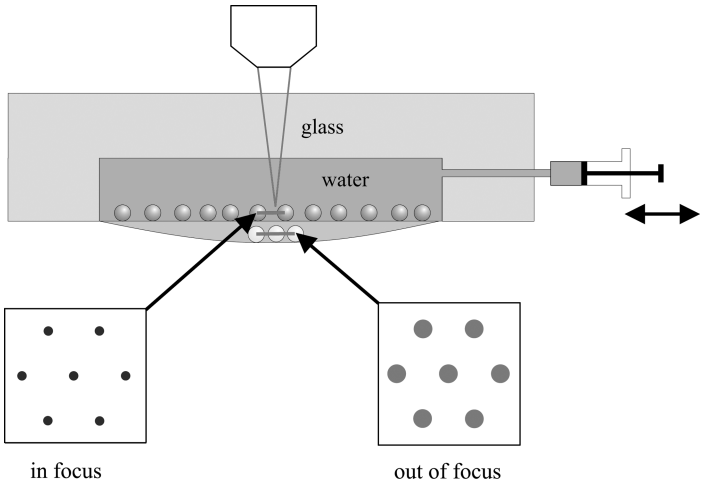

Fig. 2.10 Schematic drawing of the regulation of the interface using the projected size of the colloids. Colloids appear smallest when in focus. Deviations from the set point of projected size are corrected by the volume of the droplet using a syringe.

by compensating the loss of water due to evaporation (even if the sample is encapsulated). A computer-controlled syringe driven by a micro-stage controls the volume of the droplet and thereby the curvature of the interface. Depending on the optical components used, a resolution down to 250 nm in the vertical position of the interface in the middle of the droplet relative to the camera is achieved. An active regulation of the vertical camera position is overlaid to get a completely flat surface. The set point is the number of particles in the field of view chosen to reach a homogeneous number density profile throughout the whole sample. That is, if the interface is convex, particle density will rise in the middle of the sample due to gravity. The camera is lifted by a micro-stage, the interface gets out of focus, which is compensated by the regulation of the syringe. In this way fluctuations around the set point of particle number are suppressed below 1% over several weeks and the biggest observed particle density gradient in the horizontal plane is less than 1%. The latter regulation is done by the variation of the inclination of the whole experimental setup. The inclination is also controlled actively by micro-stages so that the resolution is in the range of $\alpha \approx 5\,\mu\text{rad}$ providing best equilibrium conditions for long time stability. The images are analyzed with a frame rate of 250 ms and the coordinates of all the particles are recorded for every time step containing the whole phase space information. The thermal activated out-of-plane motion of the colloids is in the range of a few tenths of a nanometer so the ensemble is supposed to be an ideal two-dimensional system.

2.4 Colloidal Experiments and the KTHNY Theory

2.4.1 Direct Imaging of Defect Structures

The video-microscopy technique allows physical processes related to the motion of the colloids to be directly imaged. This technique thus seems to be particularly useful for testing the KTHNY theory – a theory whose powerful predictions are all based on the simple microscopic picture of disclination and dislocation unbinding. One may wonder if it is possible to directly observe these unbinding events and to connect these observations to the breakup of translational and orientational order.

The answer to this question is far from being clear as the colloid KTHNY literature on this point is full of irritating and partly contradictory findings. A good example is the classical work of Murray and Van Winkle (1987), who clearly derived two-stage KTHNY melting from a correlation length analysis but failed to find paired dislocations in the solid phase or free dislocations

in the hexatic phase. Instead, they observed in the fluid phase islands of sixfold coordinated particles surrounded by a network of grain boundaries of fourfold, fivefold and sevenfold coordinated particles. Inside the hexatic phase, these grain boundaries did not disappear, but neighboring grains began to orient with respect to each other. A similarly contradictory result has been obtained by Tang et al. (1989). These authors were unable to observe any sort of unbinding of an isolated dislocation into disclinations, but identified a grain-boundary-induced melting mechanism with spontaneous cluster formation of dislocations and dislocation pairs and even the formation of interconnected liquid-like islands. However, they still clearly derived correlation lengths and power-law exponents in good agreement with the KTHNY theory. Kusner et al. (1994), on the other hand, found agreement with all the elements of the KTHNY theory, including its microscopic explanation of melting. Only a few dislocations paired over short distances were found in the solid phase, while in the hexatic phase free dislocations scattered uniformly throughout the images were identified. No clustering of dislocations or any sort of grain boundaries was observed. Finally, the fluid phase was characterized by a breakup of bound disclination pairs and the formation of dislocation aggregates.

A large number of Voronoi constructions of colloid configurations are presented and discussed in the paper of Marcus and Rice (1997), one of which is shown in Fig. 2.11 for a configuration inside the hexatic phase. Bound dislocation pairs occur as clusters of two fivefold and two sevenfold particles. Unbound free dislocations made up of individual tightly bound fivefold and sevenfold sites are clearly observable. Marcus and Rice analyzed whole sequences of these configurations and found that dislocations and clusters of dislocation defects appear and disappear on the time scale of successive video frames (30 ms), and that their absolute locations are temporally uncorrelated. Thermally activated bound dislocations are thus stable only over a period much shorter than 30 ms. It is the presence of a small steady-state concentration of unbound dislocations (stemming from a dissociation of these short-lived bound dislocations) that causes the slow algebraic decay of the bond orientational order in the hexatic phase.

Such Voronoi constructions of configurations were also taken by Marcus and Rice (1997) to demonstrate that there exist states with coexistence between the hexatic and fluid phases, and between the solid and hexatic phases – a result that implies that the liquid → hexatic and hexatic → solid transitions are first order, which the authors explain with the particulars of their pair potential.

A more quantitative way of analyzing direct images of colloidal configurations has been suggested by Eisenmann et al. (2005), who used these configurations to compute the probabilities of defect formation. Assuming a

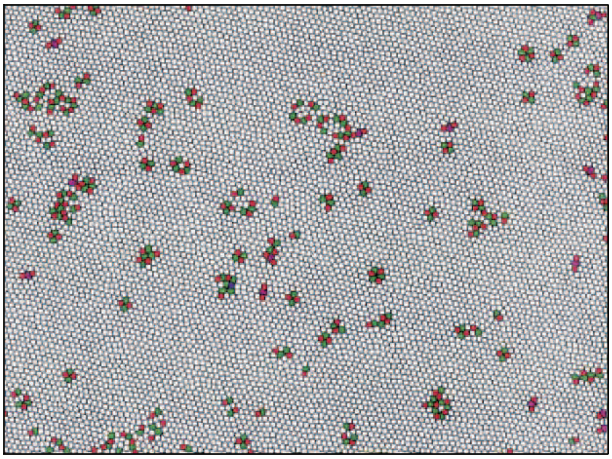

Fig. 2.11 Voronoi construction for a particle configuration with 9000 colloidal particles inside the hexatic phase. Sixfold coordinated sites are white, fivefold sites are red, sevenfold sites are green, and eightfold sites are filled green.

Boltzmann distribution one can transform these probabilities into defect interaction energies and can then test the validity of the pair interaction Hamiltonian in Eqs. (2.17) and (2.18). Figure 2.12 shows a plot of the dislocation pair energies against the inverse temperature Γ for dislocation pairs in the ground state, i.e. having the smallest separation possible on a triangular lattice. Comparison of the measured data with the solid line representing the prediction based on Eq. (2.17) reveals rather good agreement, which is the more remarkable as no adjusting parameter has been used. Equally good agreement was found with respect to the distance dependence of Eq. (2.17), but not regarding the angle dependence, where discrete lattice effects become important. Still, on the whole, the results of Eisenmann et al. (2005) clearly support the fundamental interaction Hamiltonian on which the whole KTHNY theory is based.

Summarizing this section we may say that the analysis of direct images of colloidal configurations does not always lead to unambiguous results. Murray and Van Winkle (1987), for instance, conclude from their observations that, although the microscopic ideas of dislocation and disclination unbinding seem to be too naive, the main predictions of the KTHNY theory are still in good agreement with the experimental results. Is that possible? Can a theory deliver correct results if its fundamental ideas are inappropriate? One can equally well challenge these qualitative observations, which in many cases are derived from inspecting and interpreting just a few selected images, and can ask the question whether these observations can compete with "hard"

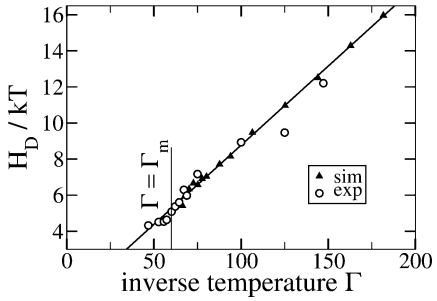

Fig. 2.12 Temperature dependence of the pair interaction energy βH_{D} of dislocation pairs in a colloidal system with $1/r^3$ pair interactions. The dislocation pairs have antiparallel Burgers vectors. Open circles: video-microscopy experiment; filled triangles: simulation; solid line: prediction according to Eqs. (2.17) and (2.18). Melting transition at $\Gamma_{\mathrm{m}} = 60$.

quantitative results that are obtained from averaging over thousands of these images. One should keep this question in mind in the following sections, where we turn to the discussion of just these quantitative results.

2.4.2 Correlations: Translational and Orientational Order

Structure Factor

To set the stage we get back to the structure factor defined in Eq. (2.2) and plotted in Fig. 2.2. Similar plots have been analyzed by Marcus and Rice (1996) for a colloidal system with hard-core repulsion. The shape of these peaks can be related to the underlying symmetry of the system (Davey et al. 1984). This is illustrated in Fig. 2.13, taken from the work of Marcus and Rice (1996); this figure shows fits of the transverse angle-dependent lineshape of $S(q)$ patterns such as those in Fig. 2.2. While the angle varies, the radius is fixed to wavevectors showing the strongest peak. There is no angular dependence for the isotropic phase (A), while the hexatic lineshape (B) agrees well with a square-root Lorentzian (solid line $S(\chi) \propto \sqrt{1/[(\chi-\alpha)^2+\beta^2]}$ with α being the peak position and β its width), and the shape in the crystalline phase (C) agrees with a simple Lorentzian function (solid line $S(\chi) \propto 1/[(\chi-\alpha)^2+\beta^2]$). These fits support the idea that the system really possesses three distinct phases, each with its own symmetry and characteristics.

Pair Correlation Functions

To study the symmetries of these phases also in real space we now turn to the pair distribution function $g(r)$ defined in Eq. (2.48) to quantify the trans-

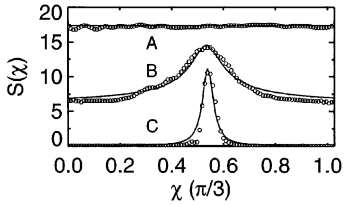

Fig. 2.13 Angular dependence of the shape of the Bragg peaks for (A) the isotropic fluid, (B) the hexatic phase, and (C) the crystal.

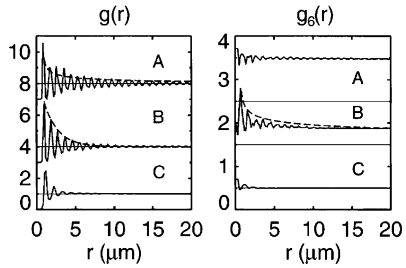

Fig. 2.14 Correlation functions $g(r)$ and $g_6(r)$ for different colloid densities. The crystalline phase (A) has quasi-long-range translational and long-range orientational order (indicated by the envelope function). The hexatic phase (B) has short-range translational and quasi-long-range orientational order; and the isotropic fluid (C) has translational and orientational short-range order. The curves have been shifted for clarity.

lational order, and to the orientational correlation function $g_6(r)$ defined in Eq. (2.49) to characterize the rotational order. In video-microscopy experiments, both correlation functions can be easily obtained from the recorded positions of the colloids. In the case of true long-range order the envelope of these correlation functions will approach a non-zero constant at large distances. As already explained this is strictly true only regarding the orientational symmetry in the crystal but not for the translational order, which is never really long-range. The translational correlation function therefore decays algebraically, i.e. like $\sim R^{-\eta_G}$, even deep inside the crystalline phase, but exponentially $\sim \mathrm{e}^{-R/\xi}$ everywhere outside the crystalline phase – see the discussion of Eqs. (2.47) and (2.48). We also recall from Section 2.2.6 that a similar algebraic decay is found also for the orientational order parameter in the hexatic phase. In the isotropic fluid, both correlation functions decay exponentially with temperature-dependent correlation lengths ξ and ξ_6. All these features can be seen in Fig. 2.14, taken from the experiment of Marcus and Rice (1996), where the particle density has been varied all the way from

the crystalline phase (A) through the hexatic phase (B) to the isotropic fluid (C).

Figure 2.15, taken from Keim et al. (2006) and Lin et al. (2006), shows similar results for the orientational correlation function produced from the video-microscopy data of colloids interacting via a magnetic dipole interaction and correlation functions of extensive simulations carried out by Lin et al. (2006). The oscillations reflect the shell structure of neighboring particles and are due to the fact that colloids with large deviations from their typical equilibrium distance are poorly correlated in their bond orientation. Also, the statistical weights of the maxima and minima are very different. Whereas the histogram of particles with distances near the maxima increases linearly with r, the corresponding histogram for the first minima shows a different dependence and is significantly smaller. This is clear; many particle pair distances contribute to the maxima, but only a few to the minima. At large distances, then, these differences are washed out and the oscillations fade away.

Figure 2.16, taken from Zahn and Maret (2000) and Lin et al. (2006), shows the same behavior, but now g_6 is calculated as a function of time (Domb and Lebowitz 1983). In the crystalline phase where only bound dislocation pairs with relatively short lifetimes are thermally excited, the bond orientation of a particle is conserved for long times. If, however, in the hexatic phase dislocation pairs dissociate and distinct dislocations diffuse through the ensemble, the bond orientation will decay on long time scales with an algebraic behavior. In the isotropic fluid free disclinations diffuse throughout the ensemble, leading to a fast exponential decay. Again, $g_6(t)$ is shown for experiment and simulation. Hence, the same qualitative behavior of the decay of the correlation is found in space and time.

2.4.3 Elasticity: Macroscopic Criteria of KTHNY Melting

We have seen in Section 2.4.1 how problematic it is to directly observe those microscopic events which the KTHNY theory postulates to determine the melting process: the dislocation and disclination unbinding. There is, however, an alternative, though less direct, way to confirm that it is these two processes that are responsible for the melting process. This way is related to the Eqs. (2.37) and (2.41).

In Section 2.2.4 we showed how the disclination unbinding temperature T_{i} can be related to the temperature-dependent Frank constant through the $72/\pi$ criterion, Eq. (2.37), and the dislocation unbinding temperature T_{m} can be related to the Young's modulus through the 16π criterion, Eq. (2.41). Both equations thus link a transition temperature to those elastic constants which are characteristic of the phases involved. Equations (2.37) and (2.41)

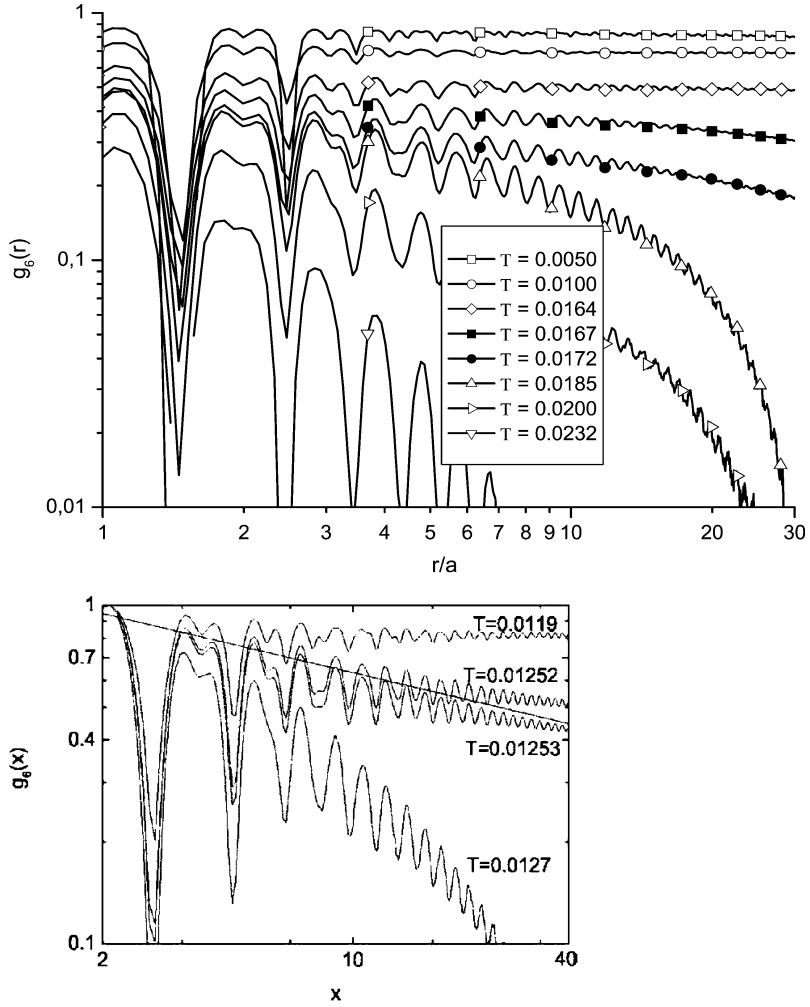

Fig. 2.15 Orientational correlation function, $g_6(r)$, for various system temperatures in a log–log plot. Experimental results are shown in the upper panel, and simulations in the lower panel. In the lower panel a curve with critical value $\eta_6 = 1/4$ is shown and $g_6(0)$ is normalized to unity. It can be seen that $lim_{r\to\infty} g_6(r) \neq 0$ in the case of long-range orientational order indicative of the crystalline phase; $g_6(r) \sim r^{-\eta_6(\Gamma)}$ in the case of quasi-long-range order typical of the hexatic phase; and $g_6(r) \sim \mathrm{e}^{-r/\xi_6(\Gamma)}$ if the order is short-range (isotropic liquid).

are, first of all, predictions that are remarkable in their simplicity, but also in their universality: whatever 2D system one considers, KTHNY predicts that the first transition is reached when the Young's modulus takes the value 16π and the second is reached when Frank's constant takes the value $72/\pi$.

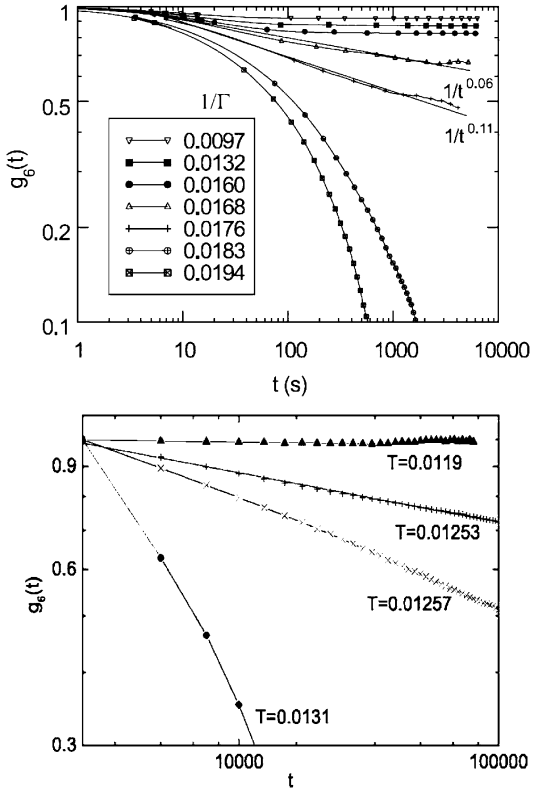

Fig. 2.16 Orientational correlation as a function of time, $g_6(t)$, for various different temperatures in a log–log plot. Experimental data are shown in the top panel, and simulation data in the lower panel. One finds the same characteristic behavior as in Fig. 2.15, but different critical exponents.

Secondly, these are obviously macroscopic criteria, as no detail of the pair potential needs to be known, only the temperature dependence of the Young's modulus and the Frank constant, which as elastic constants are macroscopic quantities. But, thirdly and most importantly in the current context, these criteria are the two mathematical statements that best summarize the microscopic picture of melting suggested by the KTHNY theory; they define the point where we get direct access to the essential KTHNY idea of defect unbinding.

To understand this latter remark, recall that Eqs. (2.37) and (2.41) were derived by searching for those temperatures where the mean defect pair distance $\langle r^2 \rangle$ in Eq. (2.31) tends to infinity. That we can derive similar criteria for both T_i and T_m is thus simply due to the fact that both the disclination–disclination interaction and the dislocation–dislocation interaction have the

same distance-dependent interaction potential in Eq. (2.28), which differ only in the prefactor c, which in turn depends on nothing but Young's modulus in one case and Frank's constant in the other case, but not on any particulars of the pair potential. We also understand that both criteria just reflect the unbinding condition $c = 4$, i.e. the temperature where the respective unbinding for each defect type is completed. In that sense, these two criteria represent the most direct way to check the microscopic principles of the KTHNY theory. If we find these criteria to be satisfied in 2D systems, then we may safely assume that these principles must be effective, irrespective of whether we are able to directly observe them in our video-microscopy images or not.

Each continuous symmetry that is broken at a phase transition to a discrete one is associated with a specific modulus of stiffness. An obvious example of this principle from everyday experience is the liquid-to-crystal transition where a non-zero shear modulus goes along with the appearance of the solid crystal. In two dimensions this is reflected by the behavior of the Young's modulus, which jumps from zero to 16π at T_{m}. As is evident from Eq. (2.9), the Young's modulus is determined by the shear modulus. Thus, also the shear modulus takes a non-zero value below T_{m}, which is in agreement with our experience that a crystal can resist shear stress. The same applies to the transition from the liquid to the hexatic phase: the Frank constant defined in Eq. (2.11) jumps from zero to $72/\pi$ at T_{i}, thus reflecting the fact that the hexatic phase, but not the liquid, can resist rotational stress.

Young's Modulus

In principle one could use the exponents of the algebraic decay of the translational correlation function in the crystalline phase, Eq. (2.43), to determine the elasticity as a function of temperature [see Zanghellini et al. (2005)], but here we will present results that are based on an alternative approach. Keim et al. (2004) describe a method to determine the elastic dispersion relation of a two-dimensional colloidal system. These relations quantify the "microscopic spring constants" of the crystal in q-space. Analyzing the low-q behavior of the longitudinal and transverse bands one can extract the Lamé coefficients λ and μ, which can then be used to determine the Young's modulus. This allows one to measure this modulus as a function of temperature and to compare it to the function $K_{\mathrm{R}}(T)$ obtained from the Halperin–Nelson recursion relations in Eq. (2.39) – thus allowing a direct check of the 16π criterion in Eq. (2.41). We present in Fig. 2.17 the results for $K_{\mathrm{R}}(T)$, which indeed approaches the universal value 16π at T_{m} (von Grünberg et al. 2004; Zanghellini et al. 2005). For the colloidal system the data points and the KTHNY prediction agree within the experimental error bars. The essential conclusion here is that, based on thermally excited phonon softening,

one would expect the Young's modulus K to cross 16π at $\Gamma = 51$, while including the additional effect of the dislocations leads to a crossing of the 16π line at a higher value of Γ ($\Gamma_{\mathrm{m}} = 60$). This difference shows that the temperature dependence of K is produced not only by interacting phonons, but near Γ_{m} also by dislocations. The data points follow the curves derived from Eq. (2.39). Note that from these observations alone nothing can be inferred about the order of the transition.

Also shown in Fig. 2.17 are the corresponding experimental and simulated curves for a 2D electron solid on the surface of liquid helium. Fisher et al. (1979) determined the temperature dependence of the shear modulus of the 2D electron solid in a computer simulation and fitted the data points to $K(\Gamma) = 0.6386(\Gamma - 30.8)$, which in Fig. 2.17 is seen to cross 16π at $\Gamma = 109.5$. The Halperin–Nelson renormalization relations [with E_{c} as free parameter – see Zanghellini et al. (2005)] leads to a correction of this value to $\Gamma = 143$. Figure 2.17 shows the experimental data points for a 2D electron system on helium as obtained by Gallet et al. (1982) from a measurement of the coupled electron–substrate transverse sound mode for three different electron densities. All three data sets pass through 16π at a common value of Γ which is close to 143, but unfortunately fail to fall onto a common curve as one would have expected. While the reason for this discrepancy remains unclear, at least one experimental data set is in good agreement with the curve given by the KTHNY theory.

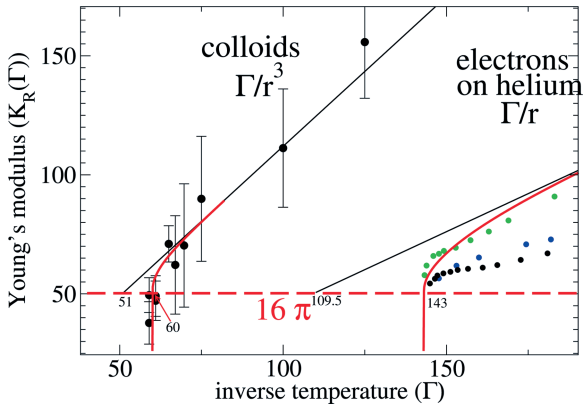

Fig. 2.17 Experimental check of the Kosterlitz–Thouless criterion of melting expressed by Eq. (2.41): the Young's modulus as a function of Γ for a system with $1/r^3$ and $1/r$ pair interactions. The theoretical curves are explained in Fig. 2.7 (bottom), and the experimental data points are for colloids with a pair interaction $1/r^3$ and electrons with pair interaction $1/r$.

It is interesting to compare the sequence of melting points predicted by Eq. (2.41) on the basis of different approximations for K in the electron system (interaction $1/r$) and the colloidal system (interaction $1/r^3$). Estimating K by the finite-T approximation, and by its renormalized values, respectively, we find in the electron system a shift of $\Gamma_{\rm m}$ at the transition from $109.5 \rightarrow 143$ while in the colloid system it shifts from $51 \rightarrow 60$. The shrinking of the shift range when going from a $1/r$ to a $1/r^3$ pair potential seems to suggest that an even more short-range potential (such as e.g. $1/r^5$) would lead to an even smaller interval for these two temperatures, making it increasingly difficult to distinguish between a defect-mediated and a phonon-mediated melting scenario. This observation is also supported by results obtained in hard-core systems (Karnchanaphanurach et al. 2000).

Frank's Constant

The procedure to use video-microscopy data for a check of the $72/\pi$ criterion, Eq. (2.37), is straightforward: one just needs to extract η_6 from the decay behavior of g_6 and can then exploit Eq. (2.52) to obtain the Frank constant K_A. This was done in Keim et al. (2006), again for 2D colloidal systems with dipolar interaction. Figure 2.18 shows the temperature dependence of K_A within the temperature range ($57 < \Gamma < 60$) of the hexatic phase. Both transition points $1/T_{\rm i} \sim \Gamma_i = 57$ and $1/T_{\rm m} \sim \Gamma_{\rm m} = 60$ have previously been deter-

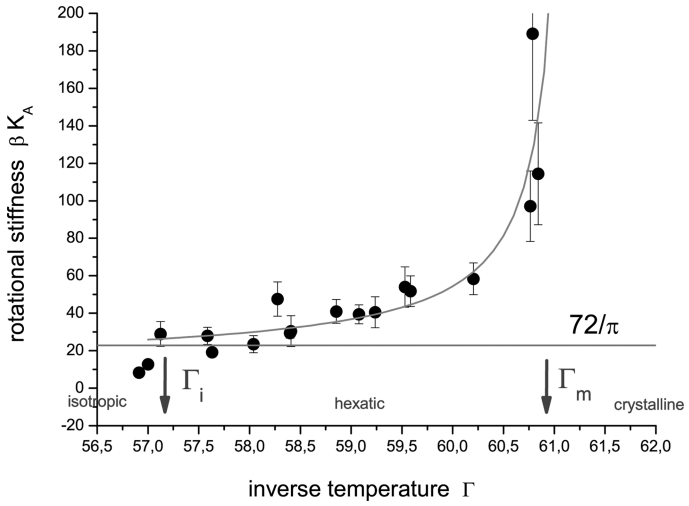

Fig. 2.18 Experimental check of the Kosterlitz–Thouless criterion of melting expressed by Eq. (2.37): Frank's constant as a function of Γ becomes $72/\pi$ at $T_{\rm i}$. At $T_{\rm m}$ it diverges, indicating that the perfect orientational symmetry of the crystalline phase is approached.

mined by a quantitative analysis of the decay behavior. Knowing Γ_i one can now determine the value of K_A at Γ_i. It indeed crosses $72/\pi$ at the transition and disappears deeper in the isotropic fluid. There is however no sudden jump to zero below Γ_i, which is an artifact probably due to the method chosen to determine K_A via η_6, as η_6 is not defined in the isotropic fluid. On the other hand, at the hexatic $\rightarrow$ crystal transition K_A diverges, since the crystal has perfect orientational order corresponding to infinite rotational stiffness. In Keim et al. (2006) the characteristic of the divergence is further analyzed.

To summarize this section, the microscopic melting mechanism of the KTHNY theory seems to be confirmed by the results presented in Figs. 2.17 and 2.18. Dislocation pair unbinding indeed takes place at T_m, otherwise the 16π criterion could not be fulfilled, and also disclination unbinding seems to happen at T_i because also the $72/\pi$ criterion is satisfied. However, we want to stress that this is not incompatible with the observations made by several groups that dislocations and disclinations may form clusters and that the unbinding events are not easy to observe directly. Still the *dominant* effect seems to be the unbinding of defect pairs.

2.5 Conclusion

This chapter is an attempt to review our current understanding of melting in two dimensions as revealed from experiments on monolayers of colloidal particles. Since the pioneering theoretical predictions of Kosterlitz, Thouless, Halperin, Nelson, and Young (KTHNY), many macro- and microscopic aspects of the melting process have been studied experimentally and numerically. Some of the early experiments, such as those on 2D electronic and atomic systems, are hampered by the failure to resolve the motion of single particles and by a coupling to the third dimension (e.g. the substrate), which is difficult to evaluate and to control. Macroscopic systems like granular layers, magnetic bubble arrays and dusty plasmas allow easy particle tracking but are intrinsically athermal and necessarily driven out of thermodynamic equilibrium. Numerical simulations still suffer to some extent from the limited number of particles and simulation times not always long enough to reach equilibrium conditions.

Because colloidal particle systems confined to monolayers minimize the above shortcomings, they have been exploited successfully over the past two decades and have revealed many new features of the melting process. The most prominent results are as follows:

- In electrically charged colloids with screened Coulomb interaction as well as magnetic or dielectric colloids with $(1/r^3)$ dipole–dipole interac-

tion, one clearly observes a two-step melting scenario from hexagonal crystals through a hexatic phase into the liquid.

- The KTHNY theory provides a prediction of the melting temperature, Γ_{m}, which can be calculated from the renormalized Lamé coefficients in agreement with experiments of dipolar systems.
- The spatial and temporal correlation functions for bond orientational order $g_6(r)$ and translational order $g(r)$ follow KTHNY predictions. When going from the crystalline through the hexatic to the liquid state, the decay of $g_6(r)$ goes from constant to algebraic to exponentially short-range, while $g(r)$ goes from algebraic to exponentially short-range to exponentially short range. The values of the exponents agree with KTHNY.
- This goes together with the appearance of bound dislocation pairs in the crystal, which dissociate at T_{m} into isolated dislocations in the hexatic phase, which at T_{i} further dissociate into isolated disclinations in the liquid state. While each defect type can be easily identified in video-microscopy images, it is difficult to directly observe the defect pair unbinding at T_{i} and T_{m} or to relate such observations to the melting process.
- The appearance of bound and free dislocations gives rise to an extra softening which adds to the usual thermal softening of the crystal produced by interaction phonons. The Young's modulus in the crystalline phase is found to fall below the usual phonon-induced value when approaching T_{m}, and decreases in agreement with the renormalization prediction of Halperin and Nelson, ultimately reaching the universal value of 16π. This finding supports the renormalization procedure of Halperin and Nelson. In fact the most quantitative way to test the KTHNY idea is to check whether the 16π criterion for the Young's modulus and the $72/\pi$ criterion for Franck´s elastic constant are satisfied at T_{m} and T_{i}, respectively, since these conditions are derived directly by the divergence of the distance of dissociating defect pairs on the microscopic level. In 2D colloidal systems with $1/r^3$ interaction, both criteria are satisfied. This result confirms the most essential idea of the KTHNY theory: that defect unbinding is the microscopic process responsible for melting.
- The distance- and temperature-dependent distributions of the dislocations in the crystalline phase allow one to directly and quantitatively check the Hamiltonian of interacting dislocations, which is the starting point of KTHNY theory.

Many of these results were obtained thanks to the 2D system of superparamagnetic colloids confined to the free air–water interface of a flat hang-

ing drop. This system is ideally 2D since the out-of-plane motions of particles are negligibly small compared to their diameter. The interparticle interaction strength – and hence the effective system temperature – can be tuned from outside by an external magnetic field. It is totally calibrated, which, combined with accurate determination of the particle trajectories, allows one to quantify all the physical properties of the system. The system size in terms of numbers of particles and observation times are larger than what can be reached in typical numerical simulations. This ensures, in particular, observations close to thermal equilibrium. Last but not least different physical quantities as obtained all from the same system can be directly quantitatively compared.

Yet, there are still quite a few open issues in 2D melting. What determines whether or not the KTHNY melting of the 2D system is preempted by a first-order transition? Numerical simulations (Strandburg 1986) on 2D systems varying the core energy in the dislocation Hamiltonian seem to suggest that the crossover from first-order melting to two-step second-order melting is controlled by the core energy E_c of a dislocation and should occur at E_c values around $2.84k_\mathrm{B}T$ (Chui 1982; Chui 1983). The physical picture is that for small enough E_c isolated disclinations are unlikely to form as dislocations start to arrange in grain boundaries at high defect densities instead of dissociating into disclinations. It is clear that more long-range interparticle potentials give rise to larger E_c and hence favor two-step melting. Our experimental observation that the distance between the observed melting temperature and the value obtained by extrapolating the curve of thermal softening (Fig. 2.17) is larger for the unscreened $1/r$ Coulomb potential than for the $1/r^3$ dipole–dipole potential is consistent with this argument. The same holds for the observation of $E_\mathrm{c} \approx 5.3k_\mathrm{B}T$ (Zanghellini et al. 2005) for the magnetic dipole system, which indeed shows two-step melting. For now, the observations of phase equilibria in the copolymer system (Angelescu et al. 2005) and the inherent structures (Chen et al. 1995; Somer et al. 1997) cannot be put into this scheme, since the core energy is not really known in those systems. It would thus be important to further quantify this issue by comparative studies on power-law potentials with different exponents and exponential potentials with different ranges. Unfortunately it seems difficult, if not impossible, to realize experiments where the range of the potential is changed under otherwise identical conditions. These investigations will therefore be a privileged playground for numerical simulation work.

Another, yet related, question concerns the role of interactions between defects. In some of the colloidal experiments (Murray and Van Winkle 1987; Tang et al. 1989) indications of weak clustering of dislocations can be seen, but this phenomenon does not seem strong enough to drive the system into phase separation. How does the clustering affect KTHNY melting? This is certainly not an academic question, as this clustering may determine the

whole melting process. Recall the observations of Murray and Van Winkle (1987) who found in the fluid phase islands of sixfold coordinated particles surrounded by a network of grain boundaries, which remained in the hexatic phase while the islands started to orient themselves with respect to each other. This observation is not compatible with the principles of a dilute gas of dislocations according to the KTHNY theory, and still all quantitative results in Murray and Van Winkle (1987) were in agreement with this theory.

Nelson and Halperin used a Hamiltonian describing dislocation pairs with four $(5, 7, 7, 5)$ coordinated particles but they stated that this is the lowest order of topological defect pairs. Higher orders of bound dislocations are possible as long as the sum of the Burgers vectors equals zero. Their dissociation at T_{m} will not change the picture of KTHNY melting but it changes the possibility of distinguishing between isolated dislocations and disclinations in the fluid phases due to the high density of topological defects. The identification of the defects is usually done by counting the nearest neighbors but that is not strictly true as one has to focus on Burgers vectors in the case of dislocations. In the isotropic liquid the concept of Burgers vectors breaks down simply because there is no lattice on which they are defined. So five- and sevenfold particles have to be identified as disclinations even if they are neighbored. Since Eq. (2.37) is derived by the divergence of the distance of disclinations finding $K_A \to 72/\pi$ the microscopic KTHNY picture is checked. Taking into account dislocations of higher order in KTHNY theory may resolve the problem of heterogeneous distribution on short length scales of dislocations at finite density.

Colloids would also be appropriate to study the role of lateral confinement on the melting process, since boundaries can be easily realized by hard mechanical walls or soft walls (Wille 2001) generated by optical tweezers (Ashkin et al. 1986). Finally colloids open a rich terrain for crystals with 2D structures other than simple hexagonal. As an example, by tilting the magnetic field out of the vertical direction in the 2D magnetic dipole experiment, i.e. away from the normal of the layer, rhombic phases have been obtained (Eisenmann et al. 2004b). This suppresses certain orientations of dislocation pairs in the crystals, stabilizes orientational correlations (thereby widening the hexatic phase) and, at larger tilt angles, results in anisotropic melting into a smectic-like phase (Eisenmann et al. 2004a). Thus, there are many more 2D phase transitions to be studied.

References

Angelescu, D. E., Harrison, C. K., Trawick, M. L., Register, R. A., and Chaikin, P. M., 2005, *Phys. Rev. Lett.* **95**(2), 025702.

Ashkin, A., Dziedzic, J., Bjorkholm, J., and Chu, S., 1986, *Opt. Lett.* **11**, 288.
Bruch, L., Cole, M., and Zaremba, E., 1997, *Physical Adsorption*. Oxford University Press, Oxford.
Chaikin, P. and Lubensky, T., 1995, *Principles of Condensed Matter Physics*, Chap. 9. Cambridge University Press, Cambridge.
Chen, K., Kaplan, T., and Mostoller, M., 1995, *Phys. Rev. Lett.* **74**, 4019.
Chui, S. T., 1982, *Phys. Rev. Lett.* **48**(14), 933.
Chui, S., 1983, *Phys. Rev. B* **28**(1), 178.
Davey, S. C., Budai, J., Goodby, J. W., Pindak, R., and Moncton, D. E., 1984, *Phys. Rev. Lett.* **53**(22), 2129.
Dimon, P., Horn, P. M., Sutton, M., Birgeneau, R. J., and Moncton, D. E., 1985, *Phys. Rev. B* **31**(1), 437.
Domb, C. and Lebowitz, J., 1983, *Phase Transitions and Critical Phenomena*, Vol. 7. Academic Press, London.
Eisenmann, C., Gasser, U., Keim, P., and Maret, G., 2004a, *Phys. Rev. Lett.* **93**, 105702.
Eisenmann, C., Keim, P., Gasser, U., and Maret, G., 2004b, *J. Phys.: Condens. Matter* **16**, 4095.
Eisenmann, C., Gasser, U., Keim, P., Maret, G., and von Grünberg, H., 2005, *Phys. Rev. Lett.* **95**, 185502.
Fisher, D., Halperin, B., and Morf, R., 1979, *Phys. Rev. B* **20**, 4692.
Gallet, F., Deville, G., Valdes, A., and Williams, F., 1982, *Phys. Rev. Lett.* **49**, 212.
Glaser, M. and Clark, N., 1993, *Adv. Chem. Phys.* **83**, 543.
Grimes, C. and Adams, G., 1979, *Phys. Rev. Lett.* **42**, 795.
Halperin, B. and Nelson, D., 1978, *Phys. Rev. Lett.* **41**(2), 121.
Heiney, P. A., Birgeneau, R. J., Brown, G. S., Horn, P. M., Moncton, D. E., and Stephens, P. W., 1982, *Phys. Rev. Lett.* **48**(2), 104.
Jaster, A., 1999, *Phys. Rev. E* **59**(3), 2594.
Karnchanaphanurach, P., Lin, B., and Rice, S. A., 2000, *Phys. Rev. E* **61**(4), 4036.
Keim, P., 2005, *PhD Thesis*, Universität Konstanz.
Keim, P., Maret, G., Herz, U., and von Grünberg, H., 2004, *Phys. Rev. Lett.* **92**, 215504.
Keim, P., Maret, G., and von Grünberg, H. H., 2006, to be published.
Kleinert, H., 1983, *Phys. Lett.* **95A**(7), 381.
Kleinert, H., 1989, *Gauge Fields in Condensed Matter*, Vol. II. World Scientific, Singapore.
Kosterlitz, J., 1974, *J. Phys. C* **7**, 1046.
Kosterlitz, J. and Thouless, D., 1973, *J. Phys. C* **6**, 1181.
Kusner, R., Mann, J., Kerins, J., and Dahm, A., 1994, *Phys. Rev. Lett.* **73**, 3113.
Kusner, R. E., Mann, J. A., and Dahm, A. J., 1995, *Phys. Rev. B* **51**(9), 5746.

Lansac, Y., Glaser, M. A., and Clark, N. A., 2006, *Phys. Rev. E* **73**(4), 041501.
Li, D. and Rice, S. A., 2005, *Phys. Rev. E* **72**(4), 041506.
Lin, S. Z., Zheng, B., and Trimper, S., 2006, *Phys. Rev. E* **73**(6), 066106.
Mak, C. H., 2006, *Phys. Rev. E* **73**(6), 065104.
Marcus, A. and Rice, S., 1996, *Phys. Rev. Lett.* **77**, 2577.
Marcus, A. and Rice, S., 1997, *Phys. Rev. E* **55**, 637.
Melzer, A., Homann, A., and Piel, A., 1996, *Phys. Rev. E* **53**(3), 2757.
Mermin, N., 1968, *Phys. Rev.* **176**(1), 250.
Mermin, N. and Wagner, H., 1966, *Phys. Rev. Lett.* **17**(22), 1133.
Murray, C. A. and Van Winkle, D. H., 1987, *Phys. Rev. Lett.* **58**, 1200.
Nabarro, F., 1967, *Theory of Dislocations*. Clarendon, Oxford.
Nelson, D. and Halperin, B., 1979, *Phys. Rev. B* **19**, 2457.
Peierls, R., 1935, *Ann. Inst. Henri Poincaré* **5**, 177.
Pindak, R., Moncton, D. E., Davey, S. C., and Goodby, J. W., 1981, *Phys. Rev. Lett.* **46**(17), 1135.
Quinn, R. A. and Goree, J., 2001, *Phys. Rev. E* **64**(5), 051404.
Reis, P. M., Ingale, R. A., and Shattuck, M. D., 2006, *Phys. Rev. Lett.* **96**(25), 258001.
Segalman, R. A., Hexemer, A., Hayward, R. C., and Kramer, E. J., 2003, *Macromolecules* **36**, 3272.
Seshadri, R. and Westervelt, R. M., 1992, *Phys. Rev. B* **46**(9), 5150.
Somer, F. L., Canright, G. S., Kaplan, T., Chen, K., and Mostoller, M., 1997, *Phys. Rev. Lett.* **79**(18), 3431.
Strandburg, K. J., 1986, *Phys. Rev. B* **34**(5), 3536.
Tang, Y., Armstrong, A. J., Mockler, R. C., and O'Sullivan, W. J., 1989, *Phys. Rev. Lett.* **62**(20), 2401.
von Grünberg, H., Keim, P., Zahn, K., and Maret, G., 2004, *Phys. Rev. Lett.* **93**, 255703.
Wille, A., 2001, *PhD Thesis*, Universität Konstanz.
Young, A., 1979, *Phys. Rev. B* **19**(4), 1855.
Zahn, K., 1997, *PhD Thesis*, Université Louis Pasteur, Strasbourg.
Zahn, K., Lenke, R., and Maret, G., 1999, *Phys. Rev. Lett.* **82**(13), 2721.
Zahn, K. and Maret, G., 2000, *Phys. Rev. Lett.* **85**(17), 3656.
Zahn, K., Méndez-Alcaraz, J., and Maret, G., 1997, *Phys. Rev. Lett.* **79**, 175.
Zanghellini, J., Keim, P., and von Grünberg, H., 2005, *J. Phys.: Condens. Matter* **17**, S3579.
Zheng, X. H. and Grieve, R., 2006, *Phys. Rev. B* **73**(6), 064205.